1 **Geometric tortuosity at invaginating rod synapses slows glutamate diffusion and shapes synaptic**
2 **responses: insights from anatomically realistic Monte Carlo simulations**
3
4 **Wallace B. Thoreson[1,2], Thomas M. Bartol[3], Nicholas H. Conoan[4], Jeffrey S. Diamond[5]**
5 [1]Truhlsen Eye Institute and Department of Ophthalmology and Visual Sciences, [2]-Pharmacology and
6 Experimental Neuroscience, University of Nebraska Medical Center, Omaha, NE 68106, USA,
7 [3]Computational Neurobiology Laboratory, The Salk Institute, La Jolla, CA 92037
8 [4]Electron Microscopy Core, University of Nebraska Medical Cetner, Omaha, NE, 68106
9 [5]Synaptic Physiology Section, Division of Intramural Research, National Institute of Neurological Diseases
10 and Strokes, Bethesda, MD 20892
11

12 **Abstract**
13   At the first synapse in the vertebrate retina, rod photoreceptor terminals form deep invaginations
14 occupied by multiple second-order rod bipolar and horizontal cell (RBP and HC) dendrites. Synaptic
15 vesicles are released into this invagination at multiple sites beneath an elongated presynaptic ribbon.
16 We investigated the impact of this complex architecture on the diffusion of synaptic glutamate and
17 activity of postsynaptic receptors. We obtained serial electron micrographs of mouse retina and
18 reconstructed four rod terminals along with their postsynaptic RBP and HC dendrites. We incorporated
19 these structures into an anatomically realistic Monte Carlo simulation of neurotransmitter diffusion and
20 receptor activation. We compared passive diffusion of glutamate in these realistic structures to existing,
21 geometrically simplified models of the synapse and found that glutamate exits anatomically realistic
22 synapses ten times more slowly than previously predicted. By comparing simulations with
23 electrophysiological recordings, we modeled synaptic activation of EAAT5 glutamate transporters in
24 rods, AMPA receptors on HC dendrites, and metabotropic glutamate receptors (mGluR6) on RRBP
25 dendrites. Our simulations suggested that ~3,000 EAAT5 transporters populate the rod presynaptic
26 membrane and that, while uptake by surrounding glial Müller cells retrieves much of the glutamate
27 released by rods, binding and uptake by EAAT5 influences RBP response kinetics. The relatively long
28 lifetime of glutamate within the cleft allows mGluR6 on RBP dendrites to temporally integrate the
29 steady stream of vesicles released at this synapse in darkness. Glutamate's tortuous diffusional path
30 through realistic synaptic geometry confers quantal variability, as release from nearby ribbon sites
31 exerts larger effects on RBP and HC receptors than release from more distant sites. While greater
32 integration may allow slower sustained release rates, added quantal variability complicates the
33 challenging task of detecting brief decreases in release produced by rod light responses at scotopic
34 threshold.
35

36 **Introduction**
37   Rod photoreceptor synaptic terminals, termed spherules due to their bulbous shape, are structurally
38 distinct from most other central synapses. The presynaptic active zone, which contains a plate-like
39 ribbon structure tethering dozens of synaptic vesicles, apposes postsynaptic dendrites of multiple
40 second-order neurons that terminate deep within an invagination into the rod spherule (Fig. 1A). Each
41 synapse is typically occupied by two RBP dendrites and two HC dendrites that extend further into the
42 invagination to flank the synaptic ridge. Absorption of even just a single photon by rhodopsin causes
43 rods to hyperpolarize, temporarily decreasing the rate at which glutamate-filled vesicles are released at
44 sites along the base of the ribbon (Moser et al., 2020; Thoreson, 2021). The resulting decrease in
45 glutamate levels in the synaptic cleft alters the activity of glutamate receptors on RBP and HC dendrites.
46 Here, we investigated how the complex architecture of this invaginating synapse influences the
47 dynamics of glutamate diffusion following its release and, consequently, the synaptic responses of
48 postsynaptic neurons.

49   Our understanding of glutamate dynamics at rod spherules has been largely shaped by work in
50 which the dimensions of the rod synapse were measured and incorporated into geometrically simplified
51 analytical diffusion models (Rao-Mirotznik et al., 1998; Rao-Mirotznik et al., 1995). The resulting
52 analysis argued that glutamate is cleared from the synaptic cleft in only a few milliseconds, suggesting
53 that vesicles act independently on post-synaptic dendrites as discrete quanta rather than being
54 integrated over time in the cleft. It also suggested that postsynaptic RBP and HC dendrites all experience
55 a similar rapid change in glutamate concentration following release of a synaptic vesicle by the rod.
56 Here, we have tested whether these results hold in a diffusion model incorporating realistic synaptic
57 architecture. We obtained block face scanning electron micrographs (SBFSEM) of mouse retina and
58 reconstructed four rod spherules along with their postsynaptic contacts. We imported these realistic
59 structures into MCell4, a Monte Carlo simulation program that represents neurotransmitter diffusion
60 and receptor/transporter kinetics as stochastic processes (Franks et al., 2002; Garcia et al., 2022; Husar,
61 2022; Kerr et al., 2008; Stiles et al., 1996). We used MCell4 to evaluate effects of synaptic geometry on
62 passive glutamate diffusion, glutamate uptake by transporters, and the activation of postsynaptic
63 glutamate receptors.
64   Simulated rod membranes were populated with type 5 excitatory amino acid transporters (EAAT5)
65 (Arriza et al., 1997; Eliasof et al., 1998; Gehlen et al., 2021; Pow and Barnett, 2000). EAAT5 retrieves a
66 fraction of synaptically released glutamate (Hasegawa et al., 2006), although most uptake appears to be
67 accomplished by EAAT1 in Müller glial membranes (Barnett and Pow, 2000; Derouiche, 1996; Eliasof et
68 al., 1998; Fyk-Kolodziej et al., 2004; Harada et al., 1998; Pow et al., 2000; Rauen et al., 1996; Rauen et
69 al., 1998; Sarthy et al., 2005). The EAAT5 transport cycle activates a large anion current ($I_{A(glu)}$) (Arriza et
70 al., 1997; Grant and Werblin, 1996; Schneider et al., 2014) that can be used as a reporter for presynaptic
71 glutamate release (Hays et al., 2020; Szmajda and Devries, 2011). An existing kinetic model of EAAT2
72 (Kolen et al., 2020) was modified to represent EAAT5 and reproduce $I_{A(glu)}$ recorded from rods in
73 response to single vesicle release events (Kolen et al., 2020). Simulated HC membranes were populated
74 with AMPA receptors (Bartol et al., 2015; Jonas et al., 1993; Lu et al., 2009), modified to reproduce
75 miniature excitatory post-synaptic currents recorded in HCs (mEPSCs). RBP membranes were populated
76 with mGluR6, which closes TRPM1 cation channels via a G_o-type G protein-mediated intracellular
77 signaling pathway (Koike et al., 2010a; Schneider et al., 2015), so that a reduction in glutamate release
78 depolarizes RBPs.
79   Our simulations revealed that glutamate takes ten times longer to exit an anatomically realistic
80 synaptic cleft than suggested previously by a geometrically simplified model (Rao-Mirotznik et al., 1998).
81 This longer lifetime at postsynaptic receptors enhances temporal integration in the RBP and suggests
82 that slower rod release rates than previously predicted can maintain the RBP membrane potential in
83 darkness. Slower diffusion kinetics also leads to greater variability in glutamate concentration transients
84 and receptor activation that depends strongly on the relative locations of the released vesicles along the
85 ribbon and the post-synaptic dendrites in the cleft. These additional sources of variability complicate
86 the challenging task facing RBPs of discriminating small rod light responses from synaptic noise, inviting
87 a reconsideration of optimal strategies for detection at scotopic threshold.
88
89 **Methods**
90 *Anatomical reconstructions and MCell simulations*
91   Serial block face images were obtained using an Apreo VS scanning electron microscope (SEM;
92 Thermo Scientific). The tissue was fixed by immersion with standard EM fixative (2% Glutaraldehyde, 2%
93 Paraformaldehyde, 0.1M Phosphate Buffer). We sectioned a volume of 14.3 × 20.6 × 24 μm. Voxel
94 dimensions are 6 × 6 × 40 nm and each image consisted of 3435 × 4000 pixels.
95   Three dimensional reconstructions were performed using Amira software. Reconstructed cell
96 membranes were converted to 3-D triangular mesh structures using the CellBlender add-on to the 3D

3

97   computer graphics program Blender (Fig. 1). The volume, surface area, and faces of the mesh structures
98   for each of the 4 rods and their post-synaptic partners are provided in Table 1. Simulations were
99   performed with these reconstructions using Monte Carlo simulation software (MCell) (Husar et al.,
100   2024) that simulates molecular diffusion as a pseudo-random walk according to an assigned diffusion
101   constant. Glutamate molecules diffuse in three dimensions in extracellular space and can interact
102   stochastically with immobile receptors and transporters located on membrane surfaces. The behavior of
103   each individual glutamate transporter and receptor was represented by stochastic transitions between
104   states within an individual Monte Carlo model.
105   To simulate EAAT5 glutamate transporters, we adjusted the kinetics, density, and location of
106   simulated transporters to reproduce the amplitude and time course of $I_{A(glu)}$ recorded in rods in response
107   to single vesicle release events. Simulated rod membranes were densely populated with EAAT5
108   (10,000/μm^2 (Hasegawa et al., 2006) and represented by a simplified model for EAAT2 (Kolen et al.,
109   2020). Glutamate binding and unbinding rates were adjusted to match the rising phase of averaged
110   single-vesicle $I_{A(glu)}$ events (Fig. S1A) and maintain the 10 μM EC_{50} measured for EAAT5 in mouse rods
111   (Thoreson and Chhunchha, 2023). We tested ON-rates from $1x10^6$ M/s to $1x10^9$ M/s. ON-rates of $1x10^8$
112   M/s and $1x10^9$ M/s produced reasonable fits to the initial inward deflection in $I_{A(glu)}$ (Fig. S1A). However,
113   simulations with an ON rate of $1x10^9$ M/s were more sensitive to EAAT5 placement than fits with $1x10^8$
114   M/s (compare panels D and E in Fig. S2) and yielded fewer channel openings than predicted from single
115   vesicle currents. To match the single-vesicle $I_{A(glu)}$ decay when using an ON-rate of $1x10^8$, we increased
116   by threefold the transition rate constant of $T_{out}*Glu \rightarrow T_{int}*Glu$.
117   We examined effects of EAAT5 location on $I_{A(glu)}$ kinetics by placing EAAT5 in four different regions:
118   rod membrane deep within the invagination adjacent to RBP tips, the neck of invagination (Neck),
119   surrounding the exit of the invagination (Exit), and distributed throughout the entire cleft (Cleft) (Fig.
120   S1C). With an ON rate of $1x10^8$ M/s, placing EAAT5 adjacent to RBP dendritic tips (turquoise) or
121   distributing transporters throughout the cleft (purple) both produced similar responses that provided a
122   reasonable match to actual $I_{A(glu)}$ events. Placing EAAT5 only in the neck of the invagination (green trace)
123   or outside the cleft (deep blue) yielded decay kinetics that were faster than actual $I_{A(glu)}$ events, as well as
124   yielding fewer channel openings. Since distributing receptors throughout the cleft yielded comparable
125   results to placing them deep within the invagination, we chose the former for subsequent simulations.
126   To estimate the number of EAAT5 transporters in rods, we began with evidence that single vesicle
127     $I_{A(glu)}$ events average 4.5 pA (Thoreson and Chhunchha, 2023). We calculated the anion driving force by
128   plotting voltage-dependent changes in the average amplitude of single vesicle $I_{A(glu)}$ events, fitting these
129   data with a straight line. The reversal potential predicted from these measurements averaged -8.2 $\pm$
130   0.62 mV (n=6 rods). The holding potential of -70 mV therefore generates a driving force of 62 mV. The
131   single channel conductance of EAAT5 measured with nitrate as a charge carrier was found to be 0.6 pS
132   (Schneider et al., 2014) and glutamate transporters in salamander rods show a single channel
133   conductance with chloride as the charge carrier of 0.7 pS (Larsson et al., 1996). SCN^- is more permeable
134   than chloride or nitrate, so we assumed a larger single channel conductance of ~1 pS. These values
135   suggest that ~72 anion channels are open at the peak of a single vesicle release event.
136   The maximum open probability of EAAT2 anion channels has been estimated at ~0.06 (Kolen et al.,
137   2020). To calculate the open probability for anion channels achieved in our simulations, we divided the
138   number of open anion channels by the total number of glutamate-bound states. We used the same rate
139   for entry into the open state from $T_{int}*Glu$ as in the earlier model for EAAT2 (9,566/s) (Kolen et al.,
140   2020). Assuming that channels are equally likely to exit the open state (i.e., open state $\rightarrow T_{int}*Glu$ =
141   9566/s), we obtain an open probability of 0.077. This seems reasonable given that EAAT5 anion currents
142   are thought to have a larger open probability than EAAT2.
143   Like other metabotropic glutamate receptors, mGluR6 forms a homodimer and both members need
144   to bind glutamate for G-protein activation (Levitz et al., 2016; Pin and Acher, 2002). We therefore

4

145 modeled mGluR6 activation as two sequential glutamate-binding steps, considering the doubly bound
146 mGluR6 dimer to be the activated receptor (Fig. S2). We assumed that the decay in the number of
147 active mGluR6 receptors (i.e., decay of the doubly bound state) following release of a single vesicle
148 should be at least as fast as the inward current evoked in RBPs by a saturating light flash (20-80%
149 increase: 25.4 $\pm$ 1.9 ms; SEM, n=19; J. Pahlberg, unpublished). As illustrated in Fig. S2, we tested
150 different rate constants and achieved a similar rate of decay in the doubly bound state using an OFF rate
151 for glutamate unbinding of 500/s (20-80%: rod 1, 27 ms; rod 2, 50 ms; rod 3, 36 ms; rod 4, 28 ms).
152 Combining this OFF rate with an ON rate for the initial glutamate binding step of $1e^8$ M/s yielded a
153 steady state EC_{50} of 14 μM (Fig. S2), matching that measured by the displacement of glutamate from
154 mGluR6 (12.3 μM; (Pin and Acher, 2002)). These parameters also yielded a slope factor of 1.4, similar to
155 changes in mGluR6-mediated responses as a function of light intensity in dark-adapted RBPs (Berntson
156 et al., 2004; Sampath and Rieke, 2004).
157   To simulate HC AMPA receptors, we used a kinetic model of AMPARs empirically derived from
158 hippocampal neurons (Jonas et al., 1993). The original parameters were developed to fit data obtained
159 at room temperature and later modified for a temperature of 34°C (Bartol et al., 2015).
160   Release from photoreceptors varies linearly with I_{Ca} (Thoreson et al., 2004) and so we estimated
161 voltage-dependence of release rates in rods from changes in I_{Ca}. For the voltage-dependence of I_{Ca}, we
162 used a Boltzmann function modified for driving force with an activation midpoint (V_{50}) obtained from a
163 sample of mouse rods (-31.5 mV; n=8) along with a reversal potential of +41 mV (Grassmeyer and
164 Thoreson, 2017) and slope factor of 9 (Haeseleer et al., 2016).
165   Other analysis and data visualization procedures were performed using Clampfit 10, GraphPad
166 Prism 9, Adobe Illustrator, and Adobe Photoshop software.
167
168 *Mice*
169   For electrophysiology studies, we used mice of both sexes aged between 4-8 weeks. Euthanasia was
170 performed by CO_2 asphyxiation followed by cervical dislocation in accordance with AVMA Guidelines for
171 the Euthanasia of Animals. Animal care and handling protocols were approved by the University of
172 Nebraska Medical Center Institutional Animal Care and Use Committee. Experiments were conducted
173 using C57BL/6J mice.
174
175 *Whole cell recordings*
176   Whole cell recordings of rods were obtained using flatmount preparations of isolated retina. Eyes
177 were enucleated after euthanizing the mouse and placed in Ames' medium (US Biological;
178 RRID:SCR_013653) bubbled with 95% O2/5% CO2. The cornea was punctured with a scalpel and the
179 anterior segment removed. The retina was isolated after cutting optic nerve attachments. We then
180 made three or four fine cuts at opposite poles and flattened the retina onto a glass slide in the perfusion
181 chamber with photoreceptors facing up. The retina was anchored in place with a brain slice harp
182 (Warner Instruments, cat. no. 64-0250). To expose rod inner segments in flatmount retina, we gently
183 touched the photoreceptors with a piece of nitrocellulose filter paper and then removed it to pull away
184 adherent outer segments. The perfusion chamber was placed on an upright fixed-stage microscope
185 (Nikon E600FN) equipped with a 60x water-immersion, long-working distance objective (1.0 NA). The
186 tissue was superfused with room temperature Ames' solution bubbled with 95% O_2/5% CO_2 at ~1 mL
187 /min.
188   Whole cell recordings were performed using either an Axopatch 200B amplifier (Molecular Devices)
189 with signals digitized by a DigiData 1550 interface (Molecular Devices) using PClamp 10 software or Heka
190 EPC-10 amplifier and Patchmaster software (Lambrecht, Pfalz, Germany). Currents were acquired with
191 filtering at 3 kHz.

192   Patch recording electrodes were pulled on a Narishige (Amityville, NY) PP-830 vertical puller using
193   borosilicate glass pipettes (1.2 mm outer diameter, 0.9 mm inner diameter with internal filament; World
194   Precision Instruments, Sarasota, FL). Pipettes had tip diameters of 1–2 μm and resistances of 10–15 MΩ.
195   Rod inner segments were targeted with positive pressure using recording electrodes mounted on
196   Huxley-Wall or motorized micromanipulators (Sutter Instruments, MP225).
197   Rod ribbons are surrounded by the glutamate transporter EAAT5 (Arriza et al. 1997; Eliasof et al.
198   1998; Hasegawa et al. 2006) and glutamate reuptake into rods by these transporters activates a large,
199   anion current ($I_{A(glu)}$) (Arriza et al., 1997; Grant and Werblin, 1996; Schneider et al., 2014). $I_{A(glu)}$ is
200   thermodynamically uncoupled from the transport process (Machtens et al., 2015). Glutamate
201   transporter anion currents can be observed in rods using Cl^- as the principal anion (Hays et al., 2020),
202   but are enhanced by replacing Cl^- with a more permeable anion like thiocyanate (SCN^-) in the patch
203   pipette (Eliasof and Jahr, 1996). The intracellular pipette solution for these experiments contained (in
204   mM): 120 KSCN, 10 TEA-Cl, 10 HEPES, 1 CaCl2, 1 MgCl2, 0.5 Na-GTP, 5 Mg-ATP, 5 EGTA, 5 phospho-
205   creatine, pH 7.3. Voltages were not corrected for a liquid junction potential of 3.9 mV.
206   To record mEPSCs from HCs, horizontal slices of retina were prepared as described elsewhere
207   (Feigenspan and Babai, 2017). Briefly, retinas were isolated and then embedded in 1.8% low gelling
208   agarose (Sigma-Aldrich). Horizontal slices (200 μm thick) were cut parallel to the plane of the retina
209   using a vibratome (Leica Microsystems) at room temperature.
210   For HC recordings, we used a pipette solution containing (in mM): 120 KGluconate, 10 TEACl, 10
211   HEPES, 5 EGTA, 1 CaCl2, 1 MgCl2, 0.5 NaGTP, 5 MgATP, 5 phosphocreatine, pH 7.2-7.3.   HCs were
212   identified visually and confirmed physiologically by the characteristic voltage-dependent currents,
213   particularly prominent A-type K^+ currents (Feigenspan and Babai, 2017). In our initial recordings, HC
214   identity was confirmed anatomically by loading the cell with the fluorescent dye Alexa 488 (Invitrogen,
215   Waltham, MA) through the patch pipette. Chemical reagents were obtained from Sigma-Aldrich unless
216   otherwise indicated.
217
218   **Results:**
219   *Model construction*
220   To create an anatomically detailed diffusion model of rod photoreceptor synapses, we first obtained
221   a series of serial block face scanning electron microscope (SBSFSEM) images from the outer retina of a
222   C57Bl6J mouse (Fig. 1A, B). By viewing consecutive sections at high magnification, we reconstructed four
223   rod spherules along with their postsynaptic HC and RBP dendrites (Fig. 1C). We then rendered the
224   reconstructed synapses as a collection of 3D surfaces (Fig. 1D) and imported them into MCell. The four
225   reconstructed terminals had the same general structure but exhibited significant variability in geometric
226   dimensions (Fig. 1E-G; Table 1).
227   Rao-Mirotznik et al. (1998) modeled the cat rod synapse as a sphere with a narrow neck for the exit.
228   We created similar models in MCell, configuring spheres with volumes to match the clefts of mouse rods
229   1 and 2 (Fig. 2A, sphere models shown at the same scale as reconstructed terminals). Like the earlier
230   model, these spheres emptied through a narrow neck (r= 0.12 μm, length = 0.1 μm).
231   Estimates of the number of glutamate molecules filling each synaptic vesicle vary widely (Orrego
232   and Villanueva, 1993; Takamori et al., 2006; Wang et al., 2019), so we chose a moderate value of 2,000
233   glutamate molecules. As mouse rod synaptic vesicles have an inner diameter of about 30 nm (Fuchs et
234   al., 2014), 2000 glutamate molecules would constitute approximately 250 mM, close to biochemical
235   measurements of purified synaptic vesicles from cortex (210 mM; (Riveros et al., 1986).

236   *Effects of synaptic geometry on passive diffusion of glutamate*
237   We first simulated the release of 2,000 glutamate molecules from points at the apexes of the two
238   spheres containing the cleft volumes of rods 1 and 2. Using a diffusion coefficient (D) describing free

6

239 diffusion of glutamate in saline (D = 8 x 10^{-6} cm^2/s; Rao-Mirotznik et al., 1998), our Monte Carlo
240 simulations predicted rapid clearance from the synaptic cleft (τ = 0.88 and 0.46 ms for spheres 1 and 2,
241 respectively; Figs. 2B,C). Using a larger sphere that matched the cleft volume of a cat rod spherule (0.21
242 μm^3; Rao-Mirotznik, et al., 1995), Monte Carlo simulations yielded a 1.6 ms time constant for glutamate
243 clearance, close to the value of 1.7 ms predicted analytically by Rao-Mirotznik et al. (1998).
244   Work at other central synapses indicates that glutamate diffusion in extracellular space at synapses
245 is slower than in free solution (Nicholson and Hrabetova, 2017; Nicholson et al., 1979; Nielsen et al.,
246 2004; Rusakov and Kullmann, 1998; Sykova, 2004). Lowering D to account for the viscous tortuosity of
247 extracellular space from 8 to 2 x 10^{-6} cm^2/s (Franks et al., 2002) slowed diffusion and consequently
248 glutamate clearance several fold (Figs. 2B, C).
249   We next analyzed the impact of realistic synaptic geometry by comparing results of the two sphere
250 models to simulations of single vesicle release in the reconstructed rod synapses. Within the realistic
251 geometry, we positioned the vesicle release site just beneath the ribbon at the center of the
252 invagination. These simulations produced even slower glutamate clearance time constants (Fig. 2B,C).
253 Notably, the cross-sectional area of extracellular space at the neck of the synaptic invaginations closely
254 approximated that of the exit from the simplified spherical models, indicating that slower clearance
255 from the reconstructed synapses was not due to greater constriction at the neck.
256   Given the larger extracellular volume fraction (α) of rod 1 compared to rod 2 (Table 1), we tested
257 the effects of this parameter on our results. To do so, we shrank the post-synaptic dendrites in rod 2 to
258 increase α from 0.11 to 0.2 and 0.3 and found that the time constant of glutamate decay remained the
259 same (Fig. 2C). Taken together, these results show that the geometric tortuosity introduced by the
260 complicated anatomy of the invaginating rod synapse dictates the dynamics of neurotransmitter
261 diffusion (Nicholson and Hrabetova, 2017; Nielsen et al., 2004; Rusakov and Kullmann, 1998).
262   Müller glial cell processes envelope rod synapses and retrieve glutamate molecules that escape the
263 cleft (Attwell et al., 1989; Rauen et al., 1998; Sarantis and Mobbs, 1992). To simulate avid Müller cell
264 uptake, we wrapped the entire rod terminal with an absorptive mesh to remove any glutamate
265 molecule that exited the synaptic cleft immediately. This absorptive perimeter had no effect on the
266 time course of glutamate clearance compared to simulations in which escaping glutamate entered a
267 large open volume (Fig. 2C). This suggests that, while Müller cell uptake is likely important for
268 maintaining a steep glutamate diffusion gradient at the mouth of the synapse, it does not directly
269 regulate the rate of glutamate clearance from the cleft.
270   We also examined passive glutamate diffusion at the other two reconstructed rod synapses. Rods 3
271 and 4 had similar cleft volumes and α compared to rod 2 (Table 1). As observed with rod 2, increasing α
272 of rods 3 and 4 did not substantially affect the rate of glutamate clearance. Although rods 2, 3 and 4 all
273 had similar cleft volumes, the rates of glutamate clearance ranged from 7.4 ms to 14 ms among them
274 (Fig. 2D). Interestingly, rods 1 and 4 exhibited similar simulated glutamate clearance rates, even though
275 rod 1 has twice the extracellular volume (Fig. 2D). These rod-to-rod differences further demonstrate the
276 powerful influence of realistic geometric tortuosity on the kinetics of glutamate diffusion within
277 invaginating rod synapses (Nicholson and Hrabetova, 2017; Rusakov and Kullmann, 1998). The combined
278 effects of viscous and geometric tortuosity slow glutamate clearance from rod synapses tenfold
279 compared to exit from a saline-filled sphere. The unexpectedly prolonged presence of glutamate in the
280 cleft prompted us to simulate its interaction with synaptic glutamate transporters and receptors.
281   To predict glutamate concentrations achieved at RBP dendrites, Rao-Mirotznik et al. modeled the
282 invaginating rod synapse as three slabs intersecting at 120 degrees, with a vesicle release site positioned
283 at the confluence of the slabs. Fig. 3A shows a schematic of the invaginating synapse with the rod

284   bipolar cell (RBP) dendrite terminating some distance below the ribbon release site while the two HC
285   dendrites flank the synaptic ridge. The model simulates this structure by using two slabs to represent
286   the extracellular space between the rod and HC membranes while the third slab represents the
287   extracellular space above a RBP terminal (Fig. 3A). We recreated this arrangement in MCell with each
288   slab consisting of two planes separated by 16 nm, then simulated release of 2000 glutamate molecules
289   at the vertex of this narrow cleft. We measured the number of glutamate molecules that entered a small
290   measurement box (15 x 100 x 200 nm) placed 70 nm from the release site (Fig. 3A). As predicted by
291   Rao-Mirotznik et al., Monte Carlo simulations of release of 2,000 molecules showed an abrupt rise and
292   rapid decline of glutamate within this region (Fig. 3C). We compared this model with a reconstructed
293   synapse by placing a measurement box (15 x 100 x 200 nm) just above a RBP dendrite in rod 3 (Fig. 3B).
294   The proximity of the measurement box to the release site minimized effects of tortuosity and so we saw
295   a similarly rapid rise and fast decay in the realistic synapse (τ_{fast} = 0.08 ms; τ_{slow} = 0.57 ms; Fig. 4C) and
296   the planar model (τ_{fast} = 0.13 ms; τ_{slow} = 0.66 ms). We converted the number of molecules in the
297   measurement regions to concentration (Fig. 3C). The peak concentration attained in the planar model
298   was slightly lower than that attained in the synapse (0.75 mM) but both are consistent with estimates of
299   synaptic glutamate levels at rod synapses obtained by use of low affinity antagonists (Cadetti et al.,
300   2008; Kim and Miller, 1993).

301   *Simulations of the glutamate transporter, EAAT5*
302   We next examined the influence of EAAT5 glutamate transporters, the principal glutamate
303   transporters in rods (Arriza et al., 1997; Eliasof et al., 1998) on glutamate lifetime in the synaptic cleft
304   (Fig. 4). Modifying a model for EAAT2 (Kolen et al., 2020), we adjusted the kinetics, density, and location
305   of simulated transporters to reproduce the amplitude and time course of $I_{A(glu)}$ recorded in rods in
306   response to single vesicle release events (Fig. 4; see Methods). The best fit to recorded EAAT5 currents
307   was obtained by placing EAAT5 in the rod membrane within the synaptic cleft (see Methods), consistent
308   with immunohistochemical localization of this protein (Gehlen et al., 2021).
309   Rod $I_{A(glu)}$ responses evoked by photolytic uncaging of glutamate or strong depolarizing voltage steps
310   reach a maximum of 12-13 pA (Mesnard et al., 2022b; Thoreson and Chhunchha, 2023), only three times
311   larger than single vesicle events, suggesting that EAAT5 transporters can be saturated by simultaneous
312   release of as few as 3 vesicles. With this constraint in mind, we simulated release of 10 vesicles and
313   progressively reduced the number of EAAT5 transporters until we achieved a state where responses
314   showed saturating responses equivalent to 3-4 vesicles. With 3,000 EAAT5 transporters distributed
315   throughout the synaptic cleft, a single vesicle stimulated ~60 open anion channel openings while
316   simultaneous release of 10 vesicles opened ~190 channels, showing saturation after release of slightly
317   more than 3 vesicles (Fig. 4D). We therefore proceeded with simulations containing 3,000 EAAT5
318   transporters in the rod membrane.
319   Fig. 4E shows the impact on synaptic glutamate levels of uptake by 3,000 EAAT5 transporters in rod
320   2. Following release of a single vesicle, the simulations show that rapid binding of glutamate to EAAT5
321   speeds the initial decline in free glutamate. This is followed by a slower decline dictated by the rate of
322   diffusion out of the synaptic cleft (τ_{fast} = 1.8 ms; τ_{slow} = 15 ms; n=12 trials). For a single vesicle release
323   event, the fast component accounted for 73% of the total decline in glutamate, consistent with binding
324   of 1,460 glutamate molecules by 3,000 transporters. Rods are capable of multivesicular release events
325   consisting of 10 or more vesicles (Hays et al., 2021). The presence of glutamate uptake by EAAT5 had
326   only small effects on the kinetics of glutamate reaching RBP dendrites. Including 3,000 EAAT5 slightly
327   accelerated glutamate decay in the measurement region placed just above RBP dendrite in the previous
328   figure (Fig. 4C; τ_{fast} = 0.12 ms; τ_{slow} = 0.56 ms). When we simulated simultaneous release of 10 vesicles,
329   the fast component corresponding to glutamate binding of EAAT5 constituted a much smaller

330   proportion of the total decline since the number of glutamate molecules (20,000) was much greater
331   than the number of transporters (Fig. 4F)
332   To measure the maximum rate of glutamate uptake by 3,000 EAAT5 transporters, we simulated
333   release of 10 vesicles inside a closed synaptic cleft (rod 2; Fig. 4F). The only exit available to glutamate
334   in this simulation was uptake by EAAT5. Uptake settled to a constant rate of 63,390 glutamate
335   molecules/s or 32 vesicles/s. Performing the same simulation in a closed sphere with the volume of rod
336   2 yielded the same uptake rate. While EAAT5 can retrieve glutamate at rates up to 32 vesicles/s,
337   glutamate declines much more rapidly when the synapse remains open, indicating that most of the
338   glutamate diffuses out of the synaptic cleft, to be retrieved by Müller glia. Thus, our evidence suggests
339   that EAAT5 in rods can take up functionally significant amounts of glutamate, as proposed by (Hasegawa
340   et al., 2006), but most of it is likely to be retrieved by extra-synaptic Müller cells, as suggested by others
341   (Harada et al., 1998; Niklaus et al., 2017; Pow et al., 2000; Rauen et al., 1998; Sarthy et al., 2005).

342   *Simulations of mGluR6 receptors on RBPs*
343   Glutamate released from rods acts at mGluR6 receptors on RBP dendrites (Nomura et al., 1994).
344   Activating these receptors triggers a signaling cascade that leads to closing of TRPM1 cation channels
345   (Koike et al., 2010b; Morgans et al., 2010). The signaling cascade is not understood in sufficient detail
346   for a complete model so we limited our model to the binding of glutamate to mGluR6. Class 3
347   metabotropic glutamate receptors--including mGluR6—form obligate homodimers in which ligand
348   binding to both members is needed to activate the G protein cascade (Levitz et al., 2016; Pin and Bettler,
349   2016). We placed 200 receptors at the tips of each of the two bipolar cell dendrites and modeled
350   receptor activation as two sequential glutamate-binding steps, considering the doubly bound mGluR6
351   dimer to be the activated receptor (Fig. S2).
352   We compared simulations of mGluR6 activity in reconstructed rods to mGluR6 activity in the
353   corresponding sphere model (Fig. 5). We placed 400 receptors in a transparent plane adjacent to a
354   release site at the apex of the sphere matching the cleft volume of rod 2 (Fig. 5A). This sphere is also
355   close to cleft volumes of rods 3 and 4 (Table 1). We tested mGluR6 binding with and without 3,000
356   EAAT5 transporters placed on the inner surface of the sphere. Nearly all of the mGluR6 receptors in the
357   sphere were rapidly bound following the release of a single glutamate-filled vesicle, and mGluR6
358   activation then decayed with a single time constant (10.1 ms; Fig. 5C, Table 2) that actually became
359   faster when EAAT5 was removed (6.6 ms; Fig. 5D, Table 2). The slower decay in the presence of EAAT5
360   suggests that the transporters buffer glutamate, delaying its escape from the cleft and prolonging its
361   interaction with mGluR6.
362   We compared these results to the kinetics and peak percentage of mGluR6 activated by a single
363   vesicle in the four reconstructed rod spherules (Fig. 5C). The peak percentage of receptors activated in
364   the two post-synaptic bipolar cells by a single vesicle ranged from 39 to 54%. For these simulations, we
365   averaged the responses of both RBPs together. When we examined each of the two bipolar cells
366   individually, we saw a greater range in the peak level of mGluR6 activation that spanned 19 to 56%, with
367   an average of 47%. In the presence of EAAT5, fitting the decay in mGluR6 activation in rods required two
368   exponentials, with slow time constants ranging from 24 to 40 ms (Fig. 5C, Table 2). In the absence of
369   EAAT5, the decay in mGluR6 activity was well fit with a single exponential. Without EAAT5, mGluR6
370   activity following release of a single vesicle attained a higher peak value and the response decayed with
371   time constants ranging from 20 to 43 ms (Fig. 5D; Table 2). Rod-to-rod differences and the slower decay
372   of mGluR6 activation in reconstructed spherules compared to a simple sphere illustrate further the
373   influence of synaptic geometry on response amplitude and kinetics.

374   *Simulations of HC AMPA Receptors*
375   HC dendrites express AMPA receptors (AMPARs) consisting of GluA2 and GluA4 subunits (Hack et al.,
376   2001; Stroh et al., 2018). These two types show similar binding kinetics (Grosskreutz et al., 2003). We

9

377   simulated HC AMPA receptors using an existing kinetic model for AMPARs (Bartol et al., 2015; Jonas et
378   al., 1993)(Fig. 6A). To assess AMPA receptor kinetics in HCs, we averaged miniature excitatory post-
379   synaptic currents (mEPSCS) recorded from 6 mouse HCs (>50 events per cell). These mEPSCs exhibited
380   rapid rise and decay phases (20-80% rise time = 0.6 ms, τ_{decay} = 0.81 ms; 95% confidence interval: 0.68 to
381   0.98 ms), as reported previously (Feigenspan and Babai, 2015). We placed 200 AMPA receptors on each
382   of the dendritic tips of the two HCs and simulated the release of a single vesicle containing 2,000
383   glutamate molecules beneath the ribbon center (Fig. 6B). Simulations in all four reconstructed synapses
384   produced a good match to the actual decay of HC mEPSCs (Fig. 6C). The rise times of simulated mEPSCs
385   were faster than actual mEPSCs, possibly due to imperfect voltage clamp of gap-junctionally coupled
386   HCs (R_s = 21.4 $\pm$ 5.75 MΩ, R_m = 245 $\pm$ 201 MΩ, C_m = 10.7 $\pm$ 8.6 pF, n=16).
387   As with mGluR6, we compared simulated AMPAR activation in the reconstructed rod synapses and
388   in the sphere model (Fig. 6D). Fig. 6D illustrates four individual simulations of mGluR6 activity in rod 3
389   obtained using different seed values. Superimposed on these four colored traces is the average AMPA
390   receptor activity in the corresponding sphere model with 200 AMPA receptors placed in a transparent
391   disc below the apical release site (n=12 seeds; gray trace, Fig. 6D). It is worth noting that unlike mGluR6
392   where almost half of the receptors are activated by a single vesicle, a much smaller percentage of AMPA
393   receptors is activated. Also, in contrast to mGluR6 activity that showed significantly different kinetics
394   between the sphere and realistic synaptic models, AMPA receptors showed the same kinetics in the
395   sphere and realistic synapse. Synaptic geometry thus has much less impact than intrinsic receptor
396   kinetics on AMPA receptor activity.

397   *Release site location and dendritic anatomy*
398   Synaptic vesicles can be released at many different locations along the base of the presynaptic
399   ribbon, suggesting that postsynaptic receptors may encounter widely varying glutamate concentration
400   waveforms depending on their location relative to each released vesicle. We examined the effects of
401   varying release site location on EAAT5 anion channel activity by simulating release at 3 different sites
402   along the ribbon: near the center and at both ends of the length of the ribbon. Within each rod, release
403   at all three sites evoked similar changes in EAAT5 anion channel activity (Fig. 7), suggesting that the
404   observed variability in single vesicle $I_{A(glu)}$ events recorded in individual rods arises primarily from
405   differences in the amount of glutamate released from each vesicle.
406   We next examined this issue from the standpoint of postsynaptic receptors in RBPs. We examined
407   mGluR6 activity in both post-synaptic RBPs individually and compared six release sites, with three sites
408   on each face of the ribbon (arrows, Fig. 8). Activation of mGluR6 in the two rods varied with release site
409   location. For example, release indicated by the magenta arrow in rod 1 evoked a much smaller response
410   (magenta traces) in bipolar cell 1 (BP1) than release at any other site. Large site-to-site differences
411   remained evident even after we increased α of rod 2 from 0.11 to 0.3 (Fig. 8, insets beneath rod 2).
412   These simulations show that differences in mGluR6 activation arise from geometric tortuosity and are
413   not due to a more tightly confined extracellular space. Some synapses exhibited smaller differences
414   between release sites. For both RBPs contacting rod 4 and BP2 beneath rod 2, mGluR6 activity was
415   similar regardless of release site location. Overall, simulations of single vesicle release events activated
416   87.4 $\pm$ 37.1 mGluR6 receptors on each bipolar cell or 43.7 $\pm$ 18.5% (median: 46.1%) of the 500 receptors
417   placed on each cell (n=48 sites, responses at each site averaged from 25 seeds).
418   AMPA receptor activity in HC dendrites was even more sensitive to release site location (Fig. 9). HCs
419   typically showed stronger responses to release sites placed on the ribbon face nearest to their
420   dendrites. Like bipolar cells, similar site-to-site differences in AMPA receptor activation remained after
421   we increased the volume fraction of rod 2 from 0.11 to 0.3, although the number of active AMPA
422   receptors diminished due to the greater glutamate dilution (Fig. 9B). On average, a single vesicle
423   activated 4.7 $\pm$ 4.0 % of the receptors (median: 3.7%; n=48 release sites), with a range from 0.14% to

10

424   16.5% (Fig. 9F). Fig. 9E shows a histogram of the peak percentage of HC AMPA receptors and RBP
425   mGluR6 activated by release of individual vesicles at different ribbon sites. While single vesicle release
426   events activated a smaller percentage of AMPA receptors than mGluR6, the c.v. for AMPA receptors as a
427   function release site location was larger (0.85) than the c.v. for mGluR6 (0.42).
428   Together, these results show that for glutamate receptors on both RBPs and HCs, release at one
429   ribbon site may have a large effect on one of the two post-synaptic cells and a small effect on the other,
430   while release at a different site may have the opposite pattern. Thus, release site location and dendritic
431   anatomy both have the potential to introduce significant sources of quantal variability at rod synapses.
432
433   **Discussion**:
434   In this study, we investigated various aspects of synaptic function at the first synapse in the visual
435   pathway using anatomically realistic Monte Carlo simulations of rod spherules. Our results show that
436   the combination of viscous and geometric tortuosity substantially delays glutamate's escape from the
437   synaptic cleft of the invaginating rod synapse. While glutamate binding and uptake by EAAT5
438   transporters help to lower glutamate levels, the persistence of glutamate in the invaginating synapse
439   prolongs RBP mGluR6 receptor activity following vesicle release. The simulations also showed the
440   significant impact of differences in cellular architecture and release site location on the amplitude and
441   kinetics of synaptic responses at RBP and HC dendrites.

442   *Effects of synaptic geometry*
443   For simplicity, Rao-Mirotznik et al. represented the invaginating rod synapse as a sphere with a
444   narrow cylindrical exit (Rao-Mirotznik et al., 1998). Our Monte Carlo simulations of diffusion within that
445   simplified geometry replicated their analytical results showing that glutamate exits such a sphere very
446   rapidly. With smaller mouse rods, glutamate departs a sphere even more quickly, with time constants of
447   less than a millisecond. Replacing the diffusion coefficient for glutamate in saline with a diffusion
448   coefficient that accounts for viscous tortuosity in the extracellular space (Nicholson and Hrabetova,
449   2017; Nicholson et al., 1979; Nielsen et al., 2004; Rusakov and Kullmann, 1998; Sykova, 2004) slowed
450   diffusion several fold. Replacing the sphere with a realistic synapse incorporating the geometric
451   tortuosity between cells slowed diffusion even further, yielding time constants for passive glutamate
452   diffusion of ~10 ms.   This slowing was not due to constriction at the neck or an excessively small
453   extracellular volume fraction in the reconstructed rod spherules. The impact of geometric tortuosity was
454   evinced further by the twofold differences in the rate of glutamate exit among rods with similar cleft
455   dimensions. While most rod spherules are outwardly similar to one another, they can differ significantly
456   in the patterns of their dendritic invaginations (Tsukamoto and Omi, 2022). Our results show that these
457   anatomic differences can have profound effects on glutamate diffusion kinetics.

458   *mGluR6*
459   To assess the effects of glutamate persistence on RBP responses, we modeled glutamate binding to
460   mGluR6 receptors.   Like other class C GPCRs, mGluR6 forms dimers in which agonists must bind both
461   members for full G protein activation (Levitz et al., 2016; Pin and Bettler, 2016). We therefore
462   considered mGluR6 active when bound to two glutamate molecules. Our simulations suggested that
463   release of glutamate from a single vesicle activates nearly half of the mGluR6 receptors on individual
464   RBPs, i.e., at the steepest part of their concentration-response curve, thereby maximizing sensitivity to
465   changes in glutamate release.
466   Our model did not incorporate downstream signaling pathways engaged by mGluR6 in which
467   glutamate binding triggers the closing of TRPM1 cation channels via interactions involving alpha and
468   beta/gamma G protein subunits (Shen et al., 2012; Xu et al., 2016). Non-linearities in the cascade could
469   also influence response amplitude and kinetics. RBPs employ a non-linear thresholding mechanism in
470   which slight changes in glutamate release cause only slight changes in TRPM1 activation whereas larger

11

471   changes in release cause disproportionately larger changes in TRPM1 activity (Field and Rieke, 2002;
472   Sampath and Rieke, 2004). This thresholding mechanism filters out small random changes in glutamate
473   release to improve detection of genuine light-evoked changes in release. The threshold for this non-
474   linearity arises from saturation of the intracellular signaling cascade, which was not included in our
475   model. However, our results suggesting that glutamate released from individual vesicles does not
476   saturate mGluR6 are consistent with these previous results.

477   *AMPA receptors*
478   We found that model parameters developed to fit AMPA receptors in hippocampal pyramidal
479   neurons yielded good fits to decay kinetics of single vesicle mEPSCs in retinal HCs (Jonas et al., 1993).
480   Both types of neurons possess GluA2 receptors (Hack et al., 2001; Stroh et al., 2018). Our simulations
481   predicted a faster rise time than observed in actual mEPSCs, but this could result from limitations in
482   voltage clamp speed of HCs that are strongly coupled to their neighbors.
483   Unitary mEPSCs in mouse HCs average 3.5 pA in amplitude (Feigenspan and Babai, 2015) and can be
484   generated by opening only 3-5 AMPA receptor channels (Hansen et al., 2021). We achieved a similar
485   number of channel openings per vesicle release event when we placed 200 receptors on each HC
486   dendrite. Comparisons of reconstructed synapses with a sphere model showed that AMPA receptor
487   kinetics are dominated by intrinsic receptor kinetics. The low affinity of AMPA receptors leads to rapid
488   de-activation and this is enhanced by rapid receptor desensitization (Hansen et al., 2021). Kinetic
489   differences among simulated mEPSCs were seen in only a few cases with exceedingly small responses
490   evoked by release at sites distant from individual HC dendrites. Rapid de-activation promotes temporal
491   independence of quanta that promotes linear summation of individual events, contributing to relatively
492   linear contrast-response curves in HCs (Burkhardt et al., 2004). This differs from the steep contrast-
493   response curves in most bipolar cells (Burkhardt et al., 2004). By providing a linear readout of rod and
494   cone membrane voltage, these mechanisms promote linear regulation of photoreceptor output via
495   inhibitory feedback from HCs (Thoreson and Mangel, 2012).

496   *EAAT5*
497   Studies by Hasegawa et al. (Hasegawa et al., 2006) suggested that presynaptic EAAT5 transporters
498   may retrieve much of the glutamate released by rods. Consistent with a role for this transporter at
499   photoreceptor synapses, genetic elimination of EAAT5 impairs the frequency responses of downstream
500   neurons (Gehlen et al., 2021). Heterologous expression of EAAT5 suggested that uptake by this
501   transporter may be too slow to contribute significantly at rod synapses, but EAAT5 expressed in rods
502   shows fast kinetics suitable for retrieval (Schneider et al., 2014; Thoreson and Chhunchha, 2023). Müller
503   cells whose processes envelope rod terminals (Sarantis and Mobbs, 1992) are also capable of significant
504   glutamate uptake mediated by EAAT1 transporters (Pow et al., 2000; Sarthy et al., 2005). Furthermore,
505   pharmacological inhibition and genetic elimination of EAAT1 impair ERG b-waves that arise from the
506   actions of photoreceptor glutamate release on bipolar cells (Harada et al., 1998; Tse et al., 2014). We
507   used our model to assess the contributions of EAAT5 vs. Müller cell uptake. To do so, we adapted an
508   existing model for EAAT2 to describe the kinetics of EAAT5 anion currents evoked by single vesicle
509   release events in rods (Kolen et al., 2020). Based on the amplitude of evoked and single vesicle $I_{A(glu)}$
510   events in rods, we concluded that there are ~3,000 EAAT5 at each rod spherule. Following glutamate
511   release, these transporters can rapidly bind up to 3,000 glutamate molecules. Glutamate transport into
512   the rod is relatively slow but capable of maintaining glutamate uptake at rates equivalent to 32
513   vesicle/s. This is close to the peak rate of sustained release by rods of 36 vesicles/s estimated from the
514   size of the readily releasable pool (90 vesicles) and the rate at which that pool can be replenished (2.5/s)
515   (Grabner et al., 2023; Grabner and Moser, 2021; Mesnard et al., 2022a; Mesnard et al., 2022b). While
516   EAAT5 may be able to keep up with much of the release in darkness, glutamate levels nevertheless
517   decline much more rapidly when the synapse remains open and Müller cell uptake is present. The higher

12

518   glutamate affinity of EAAT1 (2 μM) compared to EAAT5 (10-20 μM) can help to maintain a steep
519   gradient for glutamate diffusion out of the cleft. EAAT2 is concentrated in cones but is also found in
520   rods, where it might contribute to glutamate retrieval (Arriza et al., 1997; Eliasof et al., 1998; Gehlen et
521   al., 2021; Pow and Barnett, 2000; Tang et al., 2022). However, genetic elimination and pharmacological
522   inhibition of EAAT2 have only small effects on dark-adapted ERG b-waves (Harada et al., 1998; Tse et al.,
523   2014) suggesting minor contributions to uptake. Pharmacological inhibition of EAAT2 also has no effect
524   on $I_{A(glu)}$ in rods (Thoreson and Chhunchha, 2023). Our results therefore support the idea that Müller cell
525   uptake retrieves most of the glutamate released at rod spherules but binding of glutamate to EAAT5
526   helps speed the decline in cleft glutamate levels.
527   In addition to controlling glutamate levels in the cleft, anion currents activated by glutamate binding
528   to EAAT5 can also modify rod responses directly by altering rod membrane voltage, input resistance,
529   and Ca^{2+} channel activity. The chloride equilibrium potential in rods is ~-20 mV (Thoreson et al., 2003)
530   and so $I_{A(glu)}$ activity in darkness should have a depolarizing effect on rods. However, the stimulatory
531   effects of depolarization are opposed by direct effects of chloride efflux that reduce the open probability
532   of L-type Ca^{2+} channels via actions at specific anion-binding sites (Babai et al., 2010; Rabl et al., 2003;
533   Thoreson et al., 1997, 2000). This inhibitory effect of chloride efflux helps to limit regenerative activation
534   of Ca^{2+} channels and stabilize membrane potential in rods depolarized in darkness. We did not
535   incorporate these and other presynaptic effects into our model.

536   *Sources of synaptic variability*
537   The earlier conclusion that glutamate diffused rapidly through the invaginating synapse suggested
538   that it equilibrated rapidly throughout the cleft and that post-synaptic dendrites of rod bipolar and HC
539   dendrites all experienced similar glutamate transients in response to individual release events (Rao-
540   Mirotznik et al., 1998). However, our evidence that glutamate exits the invaginating rod synapse more
541   slowly suggests otherwise. Rod-to-rod differences in synaptic architecture led to distinct levels of
542   synaptic activity at both RBPs and HCs. We also observed differences within individual rods in the
543   activity of post-synaptic receptors on RBP and HC dendrites. This variability arises from the fact that,
544   given the same number of glutamate receptors, a more distant RBP or HC will exhibit a smaller
545   response. We also saw differences in response amplitude in individual RBPs or HCs as a function of
546   release site location. Depending on the anatomical arrangement, release at different sites along a
547   ribbon can sometimes produce large differences in mGluR6 or AMPA receptor activity in the same post-
548   synaptic cell. The lower affinity of AMPA receptors made them even more sensitive to differences in
549   release site location than mGluR6. We distributed receptors widely over the tips of RBP and HC
550   dendrites for our simulations. Confining receptor distribution to smaller regions would be expected to
551   produce even more pronounced effects of release site location on receptor activity.
552   While we saw that mGluR6 and AMPA receptor activity varied with release site location, differences
553   in release site location did not significantly affect the number of EAAT5 anion channel openings. This
554   suggests that much of the variability in single vesicle $I_{A(glu)}$ events in rods arises from variability in the
555   amount of glutamate contained within vesicles. Consistent with this, the range of volumes predicted
556   from vesicle diameters measured in electron micrographs (Fuchs et al., 2014) yields coefficients of
557   variation ranging from 0.28 to 0.44, close to the average coefficient of variation (c.v.) for single vesicle
558     $I_{A(glu)}$ events (0.39) (Thoreson and Chhunchha, 2023). This further implies that much of the variation in
559   the number of molecules per vesicle is explained by variations in diameter, implying that each vesicle
560   contains a similar concentration of glutamate.

561   *Other invaginating synapses*
562   Many other vertebrate and invertebrate neurons make invaginating synapses, which are particularly
563   abundant in Drosophila (Petralia et al., 2021). However, the invaginating spines and calyceal synapses in
564   other regions of the mammalian brain have a simpler architecture that likely limits effects of geometric

565 tortuosity. At the other end of the spectrum, invaginating synapses of cone photoreceptor cells have an
566 even more complex post-synaptic structure than rods (Sterling and Matthews, 2005) with more than a
567 dozen types of bipolar cells contacting the cone terminal at different sites (Euler et al., 2014).
568 Furthermore, HCs beneath cone terminals have glutamate receptors at both dendrites within the
569 invaginating synapse and on primary dendrites more than 1 micron away from ribbon release sites
570 (Haverkamp et al., 2000). The complex architecture of cone synapses helps to shape response kinetics,
571 with nearby bipolar cell contacts experiencing rapid glutamate changes and distant bipolar cell contacts
572 experiencing slower, smoother fluctuations (DeVries et al., 2006). Along with glutamate receptor
573 properties, the unique architecture of this synapse plays an important role in the initial filtering and
574 segregation of visual responses into different functionally-specialized, parallel bipolar cell pathways
575 (Grabner et al., 2023).

576 *Implications for rod release rates and detection of dim light by RBPs*
577 The persistence of glutamate in the invaginating synapse allows greater integration between
578 synaptic vesicle release events. For RBPs, our simulations suggest that mGluR6 receptors may remain
579 active for more than 100 ms after release of a single vesicle. Rao et al. (Rao et al., 1994) suggested that
580 release from rods in darkness must be fast enough so that release events are consistently separated by
581 time intervals shorter than a single vesicle response. Given that single vesicle events last more than 100
582 ms and assuming Poisson rates of release, this constraint can be achieved with rates of less than 25
583 quanta/s. However, Rao-Mirotznik et al. (1998) noted that release must also be fast enough to minimize
584 the possibility that a random interval might be mistaken for a genuine slowing of release produced by
585 capture of a single photon. They concluded this required release rates of 100 vesicles/s or more. This
586 exceeds the upper limit on rod release rates of 36 vesicles/s placed by the size of the readily releasable
587 pool and the rate at which that pool can be replenished (Grabner et al., 2023). One possible solution to
588 this apparent dilemma is that release may occur at more regular intervals than predicted by Poisson
589 statistics, thus allowing detection at lower release rates (Schein and Ahmad, 2005). Consistent with this
590 possibility, measurements from rods held at the typical membrane potential in darkness of –40 mV
591 suggest that they release vesicles in multivesicular bursts at regular intervals (Hays et al., 2021; Hays et
592 al., 2020).
593 Each RBP receives synaptic input from an average of 25 rods (Tsukamoto et al., 2001; Tsukamoto
594 and Omi, 2013). When detecting a single photon event, RBPs must distinguish a small reduction in
595 glutamate release occurring in only one of these 25 rods. Our results suggest several additional sources
596 of synaptic variability that may complicate this already challenging task. These include differences in rod
597 inputs arising from differences in vesicular glutamate content, geometric tortuosity of rod synapses,
598 anatomy of RBP dendrites, location of release sites along the ribbon, location of mGluR6 receptors, and
599 numbers of receptors. How are single photon responses extracted from noise in the face of this
600 variability? In addition to the possibility of regular release, RBPs employ a non-linear thresholding
601 mechanism to extract larger single photon responses from noise (Field and Rieke, 2002; Sampath and
602 Rieke, 2004). It is also possible that retinas will compensate during development for different input
603 strengths by adjusting receptor numbers and/or location to ensure that all the inputs into a RBP are
604 similar. Detailed models of rod spherules offer an opportunity to explore the limitations of these and
605 other potential mechanisms that might be employed for detection of single photon responses by RBPs.
606 Our simulations revealed surprisingly slow glutamate kinetics at invaginating rod synapses. Slow
607 kinetics allows greater integration of release events at RBP synapses that in turn allows lower release
608 rates to sustain post-synaptic activity in darkness. However, the slow kinetics of glutamate removal
609 introduces additional potential sources of quantal variability by exposing different dendrites to different

610 changes in glutamate. The mechanisms employed by rods to overcome these and other sources of
611 quantal variabillity and detect light-evoked changes in glutamate release remain to be explored fully.
612

613 **Funding**
614 This work was supported by the NINDS Intramural Research Program (NS003039 to JSD), NIH
615 EY10542 (WBT), EY32396 (WBT), NIH MMBioS P41-GM103712 (TMB), NIH CRCNS R01-MH115556 (TMB),
616 NIH CRCNS R01-MH129066 (TMB), NSF NeuroNex DBI-1707356 (TMB), and NSF NeuroNex DBI-2014862
617 (TMB). The authors would like to thank Tom Bargar of the Electron Microscopy Core Facility (EMCF) at the
618 University of Nebraska Medical Center for technical assistance. The EMCF is supported by NIH grant
619 1S10OD026790-01, state funds from the Nebraska Research Initiative (NRI), the University of Nebraska
620 Foundation, and institutionally by the Office of the Vice Chancellor for Research. The authors declare no
621 competing financial interests.
622

623 **References:**

624 Arriza, J.L., Eliasof, S., Kavanaugh, M.P., and Amara, S.G. (1997). Excitatory amino acid transporter 5, a
625 retinal glutamate transporter coupled to a chloride conductance. Proc Natl Acad Sci U S A *94*, 4155-
626 4160.
627 Attwell, D., Sarantis, M., Barbour, B., and Brew, H. (1989). Electrogenic glutamate uptake in amphibian
628 and mammalian retinal glial cells. Acta Physiol Scand Suppl *582*, 44.
629 Babai, N., Kanevsky, N., Dascal, N., Rozanski, G.J., Singh, D.P., Fatma, N., and Thoreson, W.B. (2010).
630 Anion-sensitive regions of L-type CaV1.2 calcium channels expressed in HEK293 cells. PLoS One *5*, e8602.
631 Barnett, N.L., and Pow, D.V. (2000). Antisense knockdown of GLAST, a glial glutamate transporter,
632 compromises retinal function. Invest Ophthalmol Vis Sci *41*, 585-591.
633 Bartol, T.M., Keller, D.X., Kinney, J.P., Bajaj, C.L., Harris, K.M., Sejnowski, T.J., and Kennedy, M.B. (2015).
634 Computational reconstitution of spine calcium transients from individual proteins. Front Synaptic
635 Neurosci *7*, 17.
636 Berntson, A., Smith, R.G., and Taylor, W.R. (2004). Transmission of single photon signals through a
637 binary synapse in the mammalian retina. Vis Neurosci *21*, 693-702.
638 Burkhardt, D.A., Fahey, P.K., and Sikora, M.A. (2004). Retinal bipolar cells: contrast encoding for
639 sinusoidal modulation and steps of luminance contrast. Vis Neurosci *21*, 883-893.
640 Cadetti, L., Bartoletti, T.M., and Thoreson, W.B. (2008). Quantal mEPSCs and residual glutamate: how
641 horizontal cell responses are shaped at the photoreceptor ribbon synapse. Eur J Neurosci *27*, 2575-2586.
642 Derouiche, A. (1996). Possible role of the Muller cell in uptake and metabolism of glutamate in the
643 mammalian outer retina. Vision Res *36*, 3875-3878.
644 DeVries, S.H., Li, W., and Saszik, S. (2006). Parallel processing in two transmitter microenvironments at
645 the cone photoreceptor synapse. Neuron *50*, 735-748.
646 Eliasof, S., Arriza, J.L., Leighton, B.H., Kavanaugh, M.P., and Amara, S.G. (1998). Excitatory amino acid
647 transporters of the salamander retina: identification, localization, and function. J Neurosci *18*, 698-712.
648 Eliasof, S., and Jahr, C.E. (1996). Retinal glial cell glutamate transporter is coupled to an anionic
649 conductance. Proc Natl Acad Sci U S A *93*, 4153-4158.
650 Euler, T., Haverkamp, S., Schubert, T., and Baden, T. (2014). Retinal bipolar cells: elementary building
651 blocks of vision. Nat Rev Neurosci *15*, 507-519.
652 Feigenspan, A., and Babai, N. (2015). Functional properties of spontaneous excitatory currents and
653 encoding of light/dark transitions in horizontal cells of the mouse retina. Eur J Neurosci *42*, 2615-2632.
654 Feigenspan, A., and Babai, N.Z. (2017). Preparation of Horizontal Slices of Adult Mouse Retina for
655 Electrophysiological Studies. J Vis Exp *119*, 55173.

15

656　Field, G.D., and Rieke, F. (2002). Nonlinear signal transfer from mouse rods to bipolar cells and
657　implications for visual sensitivity. Neuron *34*, 773-785.
658　Franks, K.M., Bartol, T.M., Jr., and Sejnowski, T.J. (2002). A Monte Carlo model reveals independent
659　signaling at central glutamatergic synapses. Biophys J *83*, 2333-2348.
660　Fuchs, M., Brandstatter, J.H., and Regus-Leidig, H. (2014). Evidence for a Clathrin-independent mode of
661　endocytosis at a continuously active sensory synapse. Front Cell Neurosci *8*, 60.
662　Fyk-Kolodziej, B., Qin, P., Dzhagaryan, A., and Pourcho, R.G. (2004). Differential cellular and subcellular
663　distribution of glutamate transporters in the cat retina. Vis Neurosci *21*, 551-565.
664　Garcia, J.W., Bartol, T.M., and Sejnowski, T.J. (2022). Multiscale modeling of presynaptic dynamics from
665　molecular to mesoscale. PLoS Comput Biol *18*, e1010068.
666　Gehlen, J., Aretzweiler, C., Mataruga, A., Fahlke, C., and Muller, F. (2021). Excitatory Amino Acid
667　Transporter EAAT5 Improves Temporal Resolution in the Retina. eNeuro *8*, ENEURO.0406-0421.2021.
668　Grabner, C.P., Futagi, D., Shi, J., Bindokas, V., Kitano, K., Schwartz, E.A., and DeVries, S.H. (2023).
669　Mechanisms of simultaneous linear and nonlinear computations at the mammalian cone photoreceptor
670　synapse. Nat Commun *14*, 3486.
671　Grabner, C.P., and Moser, T. (2021). The mammalian rod synaptic ribbon is essential for Cav channel
672　facilitation and ultrafast synaptic vesicle fusion. Elife *10*, e63844.
673　Grant, G.B., and Werblin, F.S. (1996). A glutamate-elicited chloride current with transporter-like
674　properties in rod photoreceptors of the tiger salamander. Vis Neurosci *13*, 135-144.
675　Grassmeyer, J.J., and Thoreson, W.B. (2017). Synaptic Ribbon Active Zones in Cone Photoreceptors
676　Operate Independently from One Another. Front Cell Neurosci *11*, 198.
677　Grosskreutz, J., Zoerner, A., Schlesinger, F., Krampfl, K., Dengler, R., and Bufler, J. (2003). Kinetic
678　properties of human AMPA-type glutamate receptors expressed in HEK293 cells. Eur J Neurosci *17*,
679　1173-1178.
680　Hack, I., Frech, M., Dick, O., Peichl, L., and Brandstatter, J.H. (2001). Heterogeneous distribution of
681　AMPA glutamate receptor subunits at the photoreceptor synapses of rodent retina. Eur J Neurosci *13*,
682　15-24.
683　Haeseleer, F., Williams, B., and Lee, A. (2016). Characterization of C-terminal Splice Variants of Cav1.4
684　Ca2+ Channels in Human Retina. J Biol Chem *291*, 15663-15673.
685　Hansen, K.B., Wollmuth, L.P., Bowie, D., Furukawa, H., Menniti, F.S., Sobolevsky, A.I., Swanson, G.T.,
686　Swanger, S.A., Greger, I.H., Nakagawa, T*., et al.* (2021). Structure, Function, and Pharmacology of
687　Glutamate Receptor Ion Channels. Pharmacol Rev *73*, 298-487.
688　Harada, T., Harada, C., Watanabe, M., Inoue, Y., Sakagawa, T., Nakayama, N., Sasaki, S., Okuyama, S.,
689　Watase, K., Wada, K*., et al.* (1998). Functions of the two glutamate transporters GLAST and GLT-1 in the
690　retina. Proc Natl Acad Sci U S A *95*, 4663-4666.
691　Hasegawa, J., Obara, T., Tanaka, K., and Tachibana, M. (2006). High-density presynaptic transporters are
692　required for glutamate removal from the first visual synapse. Neuron *50*, 63-74.
693　Haverkamp, S., Grunert, U., and Wassle, H. (2000). The cone pedicle, a complex synapse in the retina.
694　Neuron *27*, 85-95.
695　Hays, C.L., Sladek, A.L., Field, G.D., and Thoreson, W.B. (2021). Properties of multivesicular release from
696　mouse rod photoreceptors support transmission of single-photon responses. Elife *10*, e67446.
697　Hays, C.L., Sladek, A.L., and Thoreson, W.B. (2020). Resting and stimulated mouse rod photoreceptors
698　show distinct patterns of vesicle release at ribbon synapses. J Gen Physiol *152*, e202012716.
699　Husar, A., Ordyan, M., Garcia, G.C., Yancey, J.G., Saglam, A.S., Faeder, J.R., Bartol, T.M., Kennedy, M.B.,
700　and Sejnowski, T.J. (2024). MCell4 with BioNetGen: A Monte Carlo simulator of rule-based reaction-
701　diffusion systems with Python interface. PLoS Comput Biol *20*, e1011800.

702 Husar, A., Ordyan, M., Garcia, G.C., Yancey, J.G., Saglam, A.S., Faeder, J.R., Bartol, T.M., Sejnowski, T.J.
703 (2022). MCell4 with BioNetGen: A Monte Carlo Simulator of Rule-Based Reaction-Diffusion Systems with
704 Python Interface. . bioRxiv.
705 Jonas, P., Major, G., and Sakmann, B. (1993). Quantal components of unitary EPSCs at the mossy fibre
706 synapse on CA3 pyramidal cells of rat hippocampus. J Physiol *472*, 615-663.
707 Kerr, R.A., Bartol, T.M., Kaminsky, B., Dittrich, M., Chang, J.C., Baden, S.B., Sejnowski, T.J., and Stiles, J.R.
708 (2008). Fast Monte Carlo Simulation Methods for Biological Reaction-Diffusion Systems in Solution and
709 on Surfaces. SIAM J Sci Comput *30*, 3126.
710 Kim, H.G., and Miller, R.F. (1993). Properties of synaptic transmission from photoreceptors to bipolar
711 cells in the mudpuppy retina. J Neurophysiol *69*, 352-360.
712 Koike, C., Numata, T., Ueda, H., Mori, Y., and Furukawa, T. (2010a). TRPM1: a vertebrate TRP channel
713 responsible for retinal ON bipolar function. Cell Calcium *48*, 95-101.
714 Koike, C., Obara, T., Uriu, Y., Numata, T., Sanuki, R., Miyata, K., Koyasu, T., Ueno, S., Funabiki, K., Tani, A.*,
715 et al.* (2010b). TRPM1 is a component of the retinal ON bipolar cell transduction channel in the mGluR6
716 cascade. Proc Natl Acad Sci U S A *107*, 332-337.
717 Kolen, B., Kortzak, D., Franzen, A., and Fahlke, C. (2020). An amino-terminal point mutation increases
718 EAAT2 anion currents without affecting glutamate transport rates. J Biol Chem *295*, 14936-14947.
719 Larsson, H.P., Picaud, S.A., Werblin, F.S., and Lecar, H. (1996). Noise analysis of the glutamate-activated
720 current in photoreceptors. Biophys J *70*, 733-742.
721 Levitz, J., Habrian, C., Bharill, S., Fu, Z., Vafabakhsh, R., and Isacoff, E.Y. (2016). Mechanism of Assembly
722 and Cooperativity of Homomeric and Heteromeric Metabotropic Glutamate Receptors. Neuron *92*, 143-
723 159.
724 Lu, W., Shi, Y., Jackson, A.C., Bjorgan, K., During, M.J., Sprengel, R., Seeburg, P.H., and Nicoll, R.A. (2009).
725 Subunit composition of synaptic AMPA receptors revealed by a single-cell genetic approach. Neuron *62*,
726 254-268.
727 Machtens, J.P., Kortzak, D., Lansche, C., Leinenweber, A., Kilian, P., Begemann, B., Zachariae, U., Ewers,
728 D., de Groot, B.L., Briones, R.*, et al.* (2015). Mechanisms of anion conduction by coupled glutamate
729 transporters. Cell *160*, 542-553.
730 Mesnard, C.S., Barta, C.L., Sladek, A.L., Zenisek, D., and Thoreson, W.B. (2022a). Eliminating Synaptic
731 Ribbons from Rods and Cones Halves the Releasable Vesicle Pool and Slows Down Replenishment. Int J
732 Mol Sci *23*, 6429.
733 Mesnard, C.S., Hays, C.L., Barta, C.L., Sladek, A.L., Grassmeyer, J.J., Hinz, K.K., Quadros, R.M.,
734 Gurumurthy, C.B., and Thoreson, W.B. (2022b). Synaptotagmins 1 and 7 in vesicle release from rods of
735 mouse retina. Exp Eye Res *225*, 109279.
736 Morgans, C.W., Brown, R.L., and Duvoisin, R.M. (2010). TRPM1: the endpoint of the mGluR6 signal
737 transduction cascade in retinal ON-bipolar cells. Bioessays *32*, 609-614.
738 Moser, T., Grabner, C.P., and Schmitz, F. (2020). Sensory Processing at Ribbon Synapses in the Retina
739 and the Cochlea. Physiol Rev *100*, 103-144.
740 Nicholson, C., and Hrabetova, S. (2017). Brain Extracellular Space: The Final Frontier of Neuroscience.
741 Biophys J *113*, 2133-2142.
742 Nicholson, C., Phillips, J.M., and Gardner-Medwin, A.R. (1979). Diffusion from an iontophoretic point
743 source in the brain: role of tortuosity and volume fraction. Brain Res *169*, 580-584.
744 Nielsen, T.A., DiGregorio, D.A., and Silver, R.A. (2004). Modulation of glutamate mobility reveals the
745 mechanism underlying slow-rising AMPAR EPSCs and the diffusion coefficient in the synaptic cleft.
746 Neuron *42*, 757-771.
747 Niklaus, S., Cadetti, L., Vom Berg-Maurer, C.M., Lehnherr, A., Hotz, A.L., Forster, I.C., Gesemann, M., and
748 Neuhauss, S.C.F. (2017). Shaping of Signal Transmission at the Photoreceptor Synapse by EAAT2
749 Glutamate Transporters. eNeuro *4*, ENEURO.0339-0316.2017.

750 Nomura, A., Shigemoto, R., Nakamura, Y., Okamoto, N., Mizuno, N., and Nakanishi, S. (1994).
751 Developmentally regulated postsynaptic localization of a metabotropic glutamate receptor in rat rod
752 bipolar cells. Cell *77*, 361-369.
753 Orrego, F., and Villanueva, S. (1993). The chemical nature of the main central excitatory transmitter: a
754 critical appraisal based upon release studies and synaptic vesicle localization. Neuroscience *56*, 539-555.
755 Petralia, R.S., Yao, P.J., Kapogiannis, D., and Wang, Y.X. (2021). Invaginating Structures in Synapses -
756 Perspective. Front Synaptic Neurosci *13*, 685052.
757 Pin, J.P., and Acher, F. (2002). The metabotropic glutamate receptors: structure, activation mechanism
758 and pharmacology. Curr Drug Targets CNS Neurol Disord *1*, 297-317.
759 Pin, J.P., and Bettler, B. (2016). Organization and functions of mGlu and GABA(B) receptor complexes.
760 Nature *540*, 60-68.
761 Pow, D.V., and Barnett, N.L. (2000). Developmental expression of excitatory amino acid transporter 5: a
762 photoreceptor and bipolar cell glutamate transporter in rat retina. Neurosci Lett *280*, 21-24.
763 Pow, D.V., Barnett, N.L., and Penfold, P. (2000). Are neuronal transporters relevant in retinal glutamate
764 homeostasis? Neurochem Int *37*, 191-198.
765 Rabl, K., Bryson, E.J., and Thoreson, W.B. (2003). Activation of glutamate transporters in rods inhibits
766 presynaptic calcium currents. Vis Neurosci *20*, 557-566.
767 Rao-Mirotznik, R., Buchsbaum, G., and Sterling, P. (1998). Transmitter concentration at a three-
768 dimensional synapse. J Neurophysiol *80*, 3163-3172.
769 Rao-Mirotznik, R., Harkins, A.B., Buchsbaum, G., and Sterling, P. (1995). Mammalian rod terminal:
770 architecture of a binary synapse. Neuron *14*, 561-569.
771 Rao, R., Buchsbaum, G., and Sterling, P. (1994). Rate of quantal transmitter release at the mammalian
772 rod synapse. Biophys J *67*, 57-63.
773 Rauen, T., Rothstein, J.D., and Wassle, H. (1996). Differential expression of three glutamate transporter
774 subtypes in the rat retina. Cell Tissue Res *286*, 325-336.
775 Rauen, T., Taylor, W.R., Kuhlbrodt, K., and Wiessner, M. (1998). High-affinity glutamate transporters in
776 the rat retina: a major role of the glial glutamate transporter GLAST-1 in transmitter clearance. Cell
777 Tissue Res *291*, 19-31.
778 Riveros, N., Fiedler, J., Lagos, N., Munoz, C., and Orrego, F. (1986). Glutamate in rat brain cortex synaptic
779 vesicles: influence of the vesicle isolation procedure. Brain Res *386*, 405-408.
780 Rusakov, D.A., and Kullmann, D.M. (1998). Geometric and viscous components of the tortuosity of the
781 extracellular space in the brain. Proc Natl Acad Sci U S A *95*, 8975-8980.
782 Sampath, A.P., and Rieke, F. (2004). Selective transmission of single photon responses by saturation at
783 the rod-to-rod bipolar synapse. Neuron *41*, 431-443.
784 Sarantis, M., and Mobbs, P. (1992). The spatial relationship between Muller cell processes and the
785 photoreceptor output synapse. Brain Res *584*, 299-304.
786 Sarthy, V.P., Pignataro, L., Pannicke, T., Weick, M., Reichenbach, A., Harada, T., Tanaka, K., and Marc, R.
787 (2005). Glutamate transport by retinal Muller cells in glutamate/aspartate transporter-knockout mice.
788 Glia *49*, 184-196.
789 Schein, S., and Ahmad, K.M. (2005). A clockwork hypothesis: synaptic release by rod photoreceptors
790 must be regular. Biophys J *89*, 3931-3949.
791 Schneider, F.M., Mohr, F., Behrendt, M., and Oberwinkler, J. (2015). Properties and functions of TRPM1
792 channels in the dendritic tips of retinal ON-bipolar cells. Eur J Cell Biol *94*, 420-427.
793 Schneider, N., Cordeiro, S., Machtens, J.P., Braams, S., Rauen, T., and Fahlke, C. (2014). Functional
794 properties of the retinal glutamate transporters GLT-1c and EAAT5. J Biol Chem *289*, 1815-1824.
795 Shen, Y., Rampino, M.A., Carroll, R.C., and Nawy, S. (2012). G-protein-mediated inhibition of the Trp
796 channel TRPM1 requires the Gbetagamma dimer. Proc Natl Acad Sci U S A *109*, 8752-8757.

18

797 Sterling, P., and Matthews, G. (2005). Structure and function of ribbon synapses. Trends Neurosci *28*, 20-
798 29.
799 Stiles, J.R., Van Helden, D., Bartol, T.M., Jr., Salpeter, E.E., and Salpeter, M.M. (1996). Miniature endplate
800 current rise times less than 100 microseconds from improved dual recordings can be modeled with
801 passive acetylcholine diffusion from a synaptic vesicle. Proc Natl Acad Sci U S A *93*, 5747-5752.
802 Stroh, S., Puller, C., Swirski, S., Holzel, M.B., van der Linde, L.I.S., Segelken, J., Schultz, K., Block, C.,
803 Monyer, H., Willecke, K*., et al.* (2018). Eliminating Glutamatergic Input onto Horizontal Cells Changes the
804 Dynamic Range and Receptive Field Organization of Mouse Retinal Ganglion Cells. J Neurosci *38*, 2015-
805 2028.
806 Sykova, E. (2004). Diffusion properties of the brain in health and disease. Neurochem Int *45*, 453-466.
807 Szmajda, B.A., and Devries, S.H. (2011). Glutamate spillover between mammalian cone photoreceptors. J
808 Neurosci *31*, 13431-13441.
809 Takamori, S., Holt, M., Stenius, K., Lemke, E.A., Gronborg, M., Riedel, D., Urlaub, H., Schenck, S., Brugger,
810 B., Ringler, P*., et al.* (2006). Molecular anatomy of a trafficking organelle. Cell *127*, 831-846.
811 Tang, F.S., Yuan, H.L., Liu, J.B., Zhang, G., Chen, S.Y., and Ke, J.B. (2022). Glutamate Transporters EAAT2
812 and EAAT5 Differentially Shape Synaptic Transmission from Rod Bipolar Cell Terminals. eNeuro *9*,
813 ENEURO.0074-0022.2022.
814 Thoreson, W.B. (2021). Transmission at rod and cone ribbon synapses in the retina. Pflugers Arch *473*,
815 1469-1491.
816 Thoreson, W.B., Bryson, E.J., and Rabl, K. (2003). Reciprocal interactions between calcium and chloride
817 in rod photoreceptors. J Neurophysiol *90*, 1747-1753.
818 Thoreson, W.B., and Chhunchha, B. (2023). EAAT5 glutamate transporter rapidly binds glutamate with
819 micromolar affinity in mouse rods. J Gen Physiol *155*.
820 Thoreson, W.B., and Mangel, S.C. (2012). Lateral interactions in the outer retina. Prog Retin Eye Res *31*,
821 407-441.
822 Thoreson, W.B., Nitzan, R., and Miller, R.F. (1997). Reducing extracellular Cl- suppresses
823 dihydropyridine-sensitive Ca2+ currents and synaptic transmission in amphibian photoreceptors. J
824 Neurophysiol *77*, 2175-2190.
825 Thoreson, W.B., Nitzan, R., and Miller, R.F. (2000). Chloride efflux inhibits single calcium channel open
826 probability in vertebrate photoreceptors: chloride imaging and cell-attached patch-clamp recordings. Vis
827 Neurosci *17*, 197-206.
828 Thoreson, W.B., Rabl, K., Townes-Anderson, E., and Heidelberger, R. (2004). A highly Ca2+-sensitive pool
829 of vesicles contributes to linearity at the rod photoreceptor ribbon synapse. Neuron *42*, 595-605.
830 Tse, D.Y., Chung, I., and Wu, S.M. (2014). Pharmacological inhibitions of glutamate transporters EAAT1
831 and EAAT2 compromise glutamate transport in photoreceptor to ON-bipolar cell synapses. Vision Res
832 *103*, 49-62.
833 Tsukamoto, Y., Morigiwa, K., Ueda, M., and Sterling, P. (2001). Microcircuits for night vision in mouse
834 retina. J Neurosci *21*, 8616-8623.
835 Tsukamoto, Y., and Omi, N. (2013). Functional allocation of synaptic contacts in microcircuits from rods
836 via rod bipolar to AII amacrine cells in the mouse retina. J Comp Neurol *521*, 3541-3555.
837 Tsukamoto, Y., and Omi, N. (2022). Multiple Invagination Patterns and Synaptic Efficacy in Primate and
838 Mouse Rod Synaptic Terminals. Invest Ophthalmol Vis Sci *63*, 11.
839 Wang, Y., Fathali, H., Mishra, D., Olsson, T., Keighron, J.D., Skibicka, K.P., and Cans, A.S. (2019). Counting
840 the Number of Glutamate Molecules in Single Synaptic Vesicles. J Am Chem Soc *141*, 17507-17511.
841 Xu, Y., Orlandi, C., Cao, Y., Yang, S., Choi, C.I., Pagadala, V., Birnbaumer, L., Martemyanov, K.A., and
842 Vardi, N. (2016). The TRPM1 channel in ON-bipolar cells is gated by both the alpha and the betagamma
843 subunits of the G-protein Go. Sci Rep *6*, 20940.

844

19

Figures:
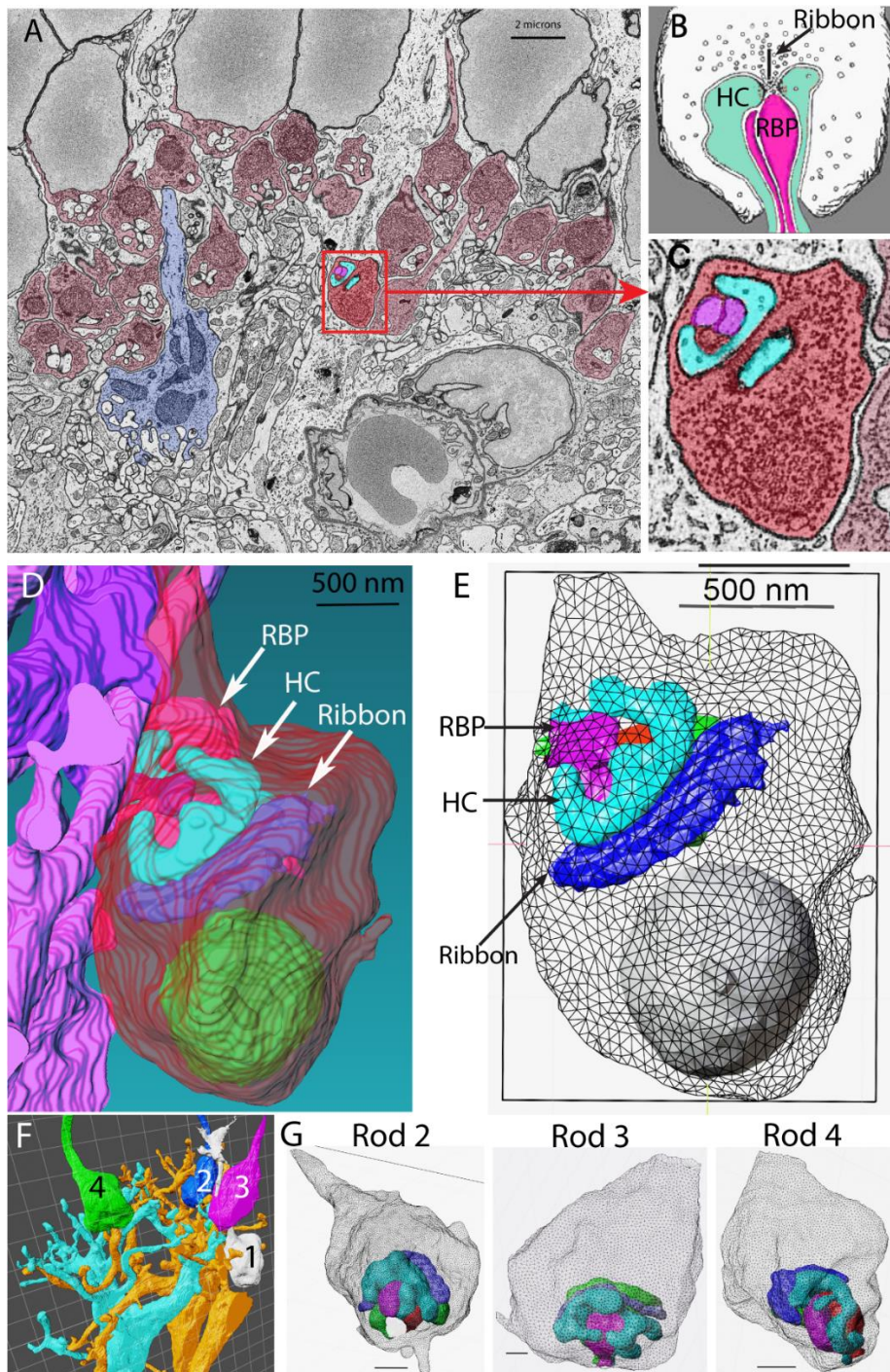
Fig. 1. Model construction. A. Example serial block face scanning electron micrograph. Rod terminals colored in red; cone terminal colored in blue. Rod 1 used for reconstruction is shown in brighter red. B. Diagram of an invaginating rod synapse. Vesicles surround the synaptic ribbon. Rod bipolar cell (RBP) dendrites are magenta and HC dendrites are turquoise. Modified under a Creative Commons License from Webvision (http://webvision.med.utah.edu/) C. Magnified image of rod 1. Post-synaptic HC dendrites are turquoise and RBP dendrites magenta. D. Reconstructed rod 1 terminal along with HC and

20

853   RBP dendrites. The synaptic ribbon (dark blue) and mitochondrion (green) are also shown. E. Mesh
854   structures of the same cells. F. Illustration of four reconstructed rod spherules (rods 1-4) with two RBPs
855   (blue and yellow). G. Mesh structures of rods 2-4 along with the post-synaptic HC and RBP dendrites.
856   Details of these mesh structures are provided in Table 1.

857
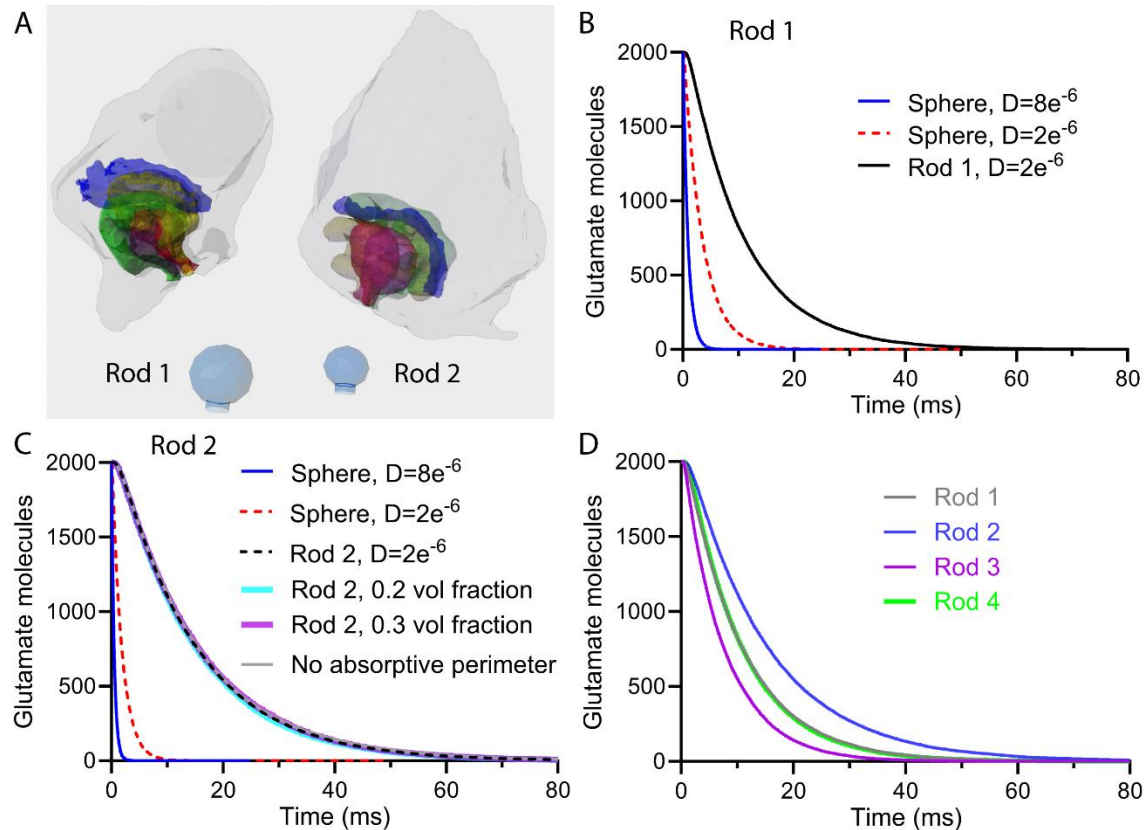
Fig. 2. Simulations of passive glutamate diffusion comparing reconstructed rod spherules with simplified
models that represented the extracellular synaptic volume as a sphere with a narrow neck for an exit. A.
Illustration of reconstructed rod spherules 1 and 2. HC dendrites are yellow and green, bipolar cell
dendrites are red and magenta, and ribbons are blue. Below each spherule is the corresponding sphere
model containing the same extracellular volume shown at the same scale. B. Plot of the number of
glutamate molecules that remained after release of a vesicle in the synaptic cleft of rod 1 (D = 2 x 10^{-6}
cm^2/s, black line) or a sphere with the same extracellular volume (D = 8 x 10^{-6} cm^2/s, blue line; D = 2 x 10^{-6} cm^2/s, dashed red line). We simulated release in rod 1 at a site just beneath the center of the ribbon.
C. Graph of the glutamate decline in a sphere with the same extracellular volume as the invaginating
synapse of rod 2 (D = 8 x 10^{-6} cm^2/s, blue line; D = 2 x 10^{-6} cm^2/s, dashed red line). This graph also shows
the decline in glutamate following release of a vesicle beneath the center of the ribbon in rod 2 with
volume fractions of 0.11 (D = 2 x 10^{-6} cm^2/s, black line), 0.2 (turquoise line), and 0.3 (purple line).
Eliminating an absorptive perimeter that simulates avid Muller cell uptake had no effect on the time
course of decay (gray trace). D. Comparison of passive glutamate decline in the four rod spherules.
Fitting the decays with single exponentials yielded the following time constants: rod 1: 10.64 ms, rod 2:
14.10 ms, rod3: 7.45 ms, rod 10: 8.89 ms. Each trace is an average of 12 simulations run using different
seed values.

21
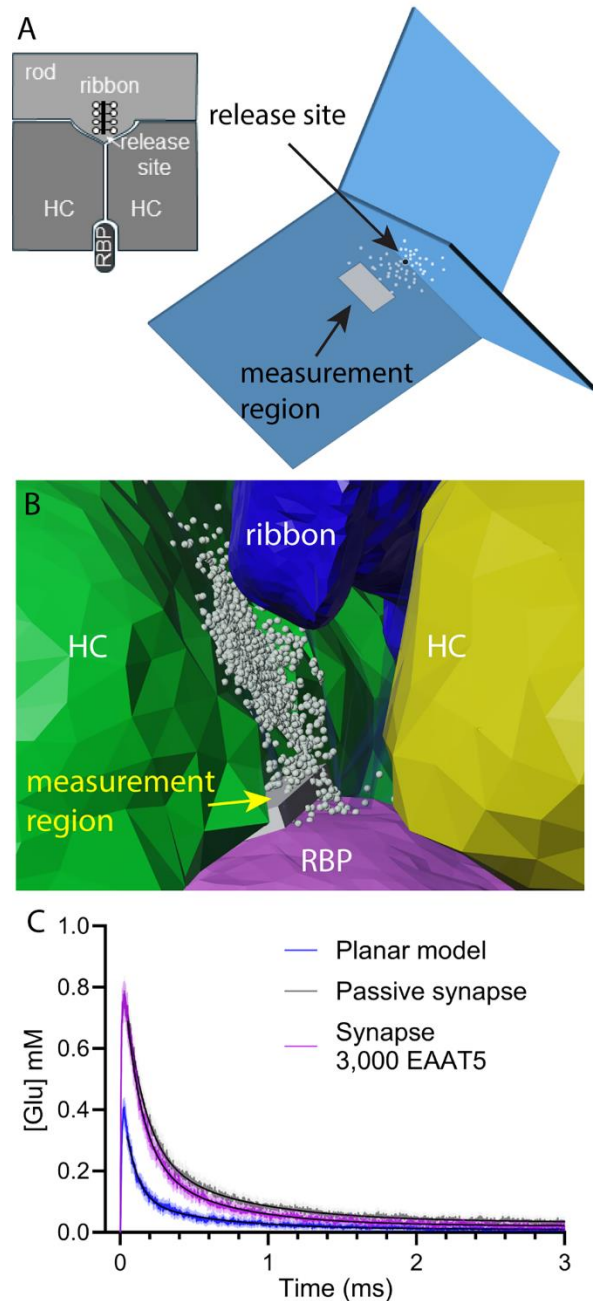
Fig. 3. Comparing glutamate kinetics between a planar model and reconstructed rod spherule. A. Schematic representation of the invaginating rod synapse with two horizontal cell (HC) dendrites flanking the synaptic ridge (upper left). A rod bipolar cell dendrite (RBP) is shown terminating beneath the ribbon release site of the rod. The image at the lower right illustrates a simplified planar model of this synaptic arrangement consisting of three slabs intersecting at an angle of 120 degrees. Each slab involves two planes separated by 16 nm to simulate a synaptic cleft. We simulated release of 2000 glutamate molecules at the vertex of this narrow cleft. We measured the number of glutamate molecules that entered a small measurement region (gray box, 15 x 100 x 200 nm) with the leading edge placed 70 nm from the release site. B. Illustration of the reconstructed rod 3 synapse with a

22

885   measurement region (gray box, 15 x 100 x 200 nm) placed just above a RBP dendrite (purple). HC
886   dendrites are shown in yellow and green. The ribbon is shown in dark blue. Glutamate molecules are
887   white. C. Monte Carlo simulations of single vesicle release showed an abrupt rise and rapid decline of
888   glutamate in measurement regions in both the planar model and reconstructed synapse. The peak
889   concentration of glutamate reached 0.4 mM in the planar model and 0.75 mM in the synapse. Decay
890   kinetics were fit with two exponentials. Planar model: τ_{fast} = 0.08 ms; τ_{slow} = 0.57 ms. Passive glutamate
891   decay in the reconstructed synapse: τ_{fast} = 0.13 ms; τ_{slow} = 0.66 ms. Decay in the reconstructed synapse
892   in the presence of active uptake by 3,000 EAAT5: τ_{fast} = 0.12 ms; τ_{slow} = 0.56 ms. Each trace is an average
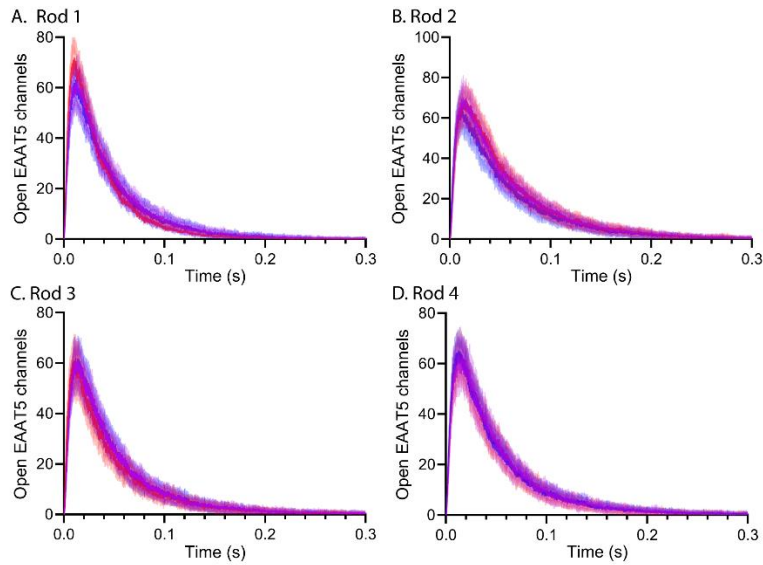893   of 12 simulations run using different seed values.
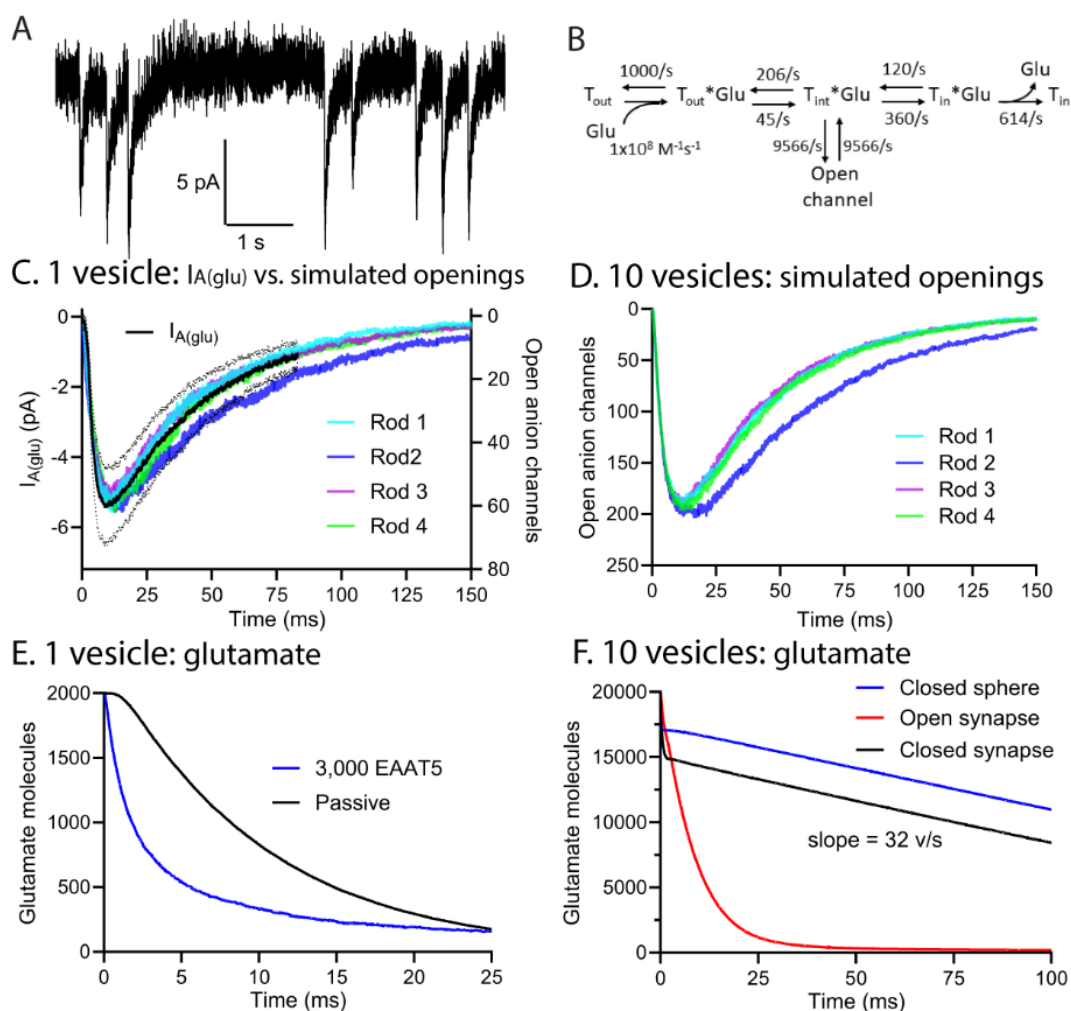
894

895   Fig. 4. Simulations of EAAT5 anion channel activity. A. Example of EAAT5 anion currents evoked by
896   single vesicle release events in a rod. B. Reaction scheme for EAAT5 (modified from a model for
897   EAAT2)(Kolen et al., 2020). C. Colored traces show the average simulated EAAT5 anion channel activity
898   in four rods following release of a single vesicle. Black trace shows the average change in $I_{A(glu)}$ ($\pm$ S.D.)
899   evoked by single vesicle release events in 15 rods (7-72 events/rod). D. EAAT5 anion channel activity
900   evoked in four rods by simulating simultaneous release of 10 vesicles. E. Comparison of the decline in
901   glutamate molecules following simulated release of a single vesicle with (blue trace) and without (black
902   trace) 3,000 EAAT5 transporters in rod 2. F. Graph of the decline in glutamate following simultaneous

23

903 release of 10 vesicles in rod 2 with open (red trace) or closed (black trace) exits at the mouth of the
904 synapse. The decline in a closed sphere with the same volume as rod 2 is plotted for comparison (blue
905 trace). All simulations are the average of 12 runs with different seed values.
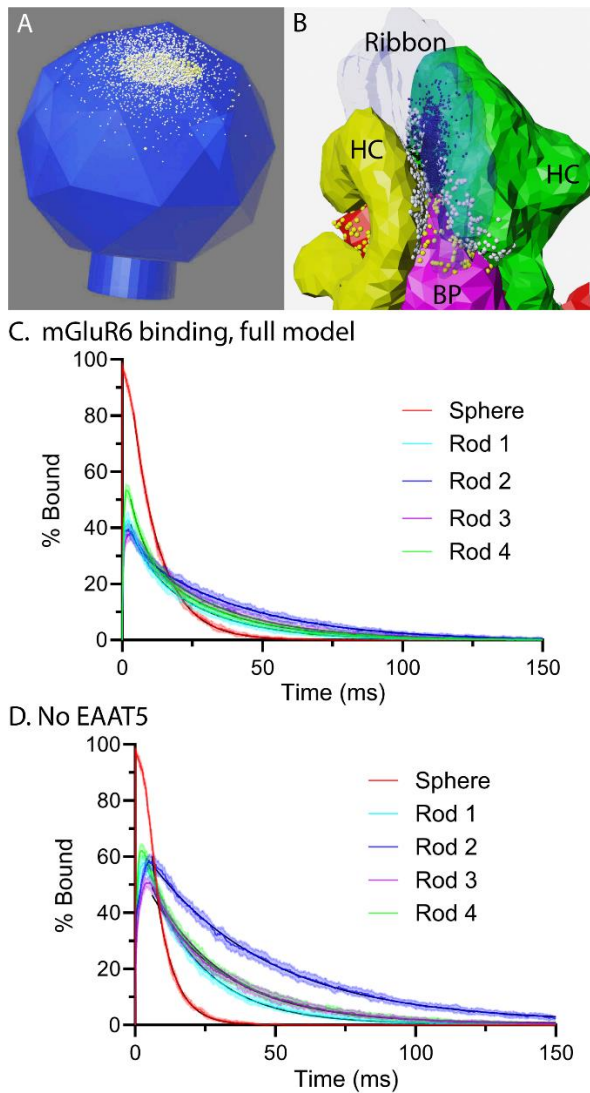

906
907 Fig. 5. Activation of mGluR6 declines more slowly in rod spherules than a similar size sphere with
908 narrow neck. A. Illustration of the sphere model for rod 2 showing 200 mGluR6 (yellow spheres) in a
909 transparent plane just beneath a release site at the apex. Glutamate molecules following release of a
910 vesicle are shown in white. B. Illustration of rod 1 with mGluR6 (yellow spheres) on bipolar cell (BP)
911 dendrites (purple and red). Glutamate molecules are white when in front of the semi-transparent
912 ribbon and shaded when behind the ribbon. C. Activation of mGluR6 in the sphere and the four rod
913 spherules in the presence of 3,000 EAAT5. The decay time courses in reconstructed rods were fit with
914 two exponentials. Decay in the sphere was fit with a single exponential. Best fit time constants are given
915 in Table 2. D. Activation of mGluR6 in the sphere and four rod spherules in the absence of EAAT5. All
916 simulations in this figure are the average of 25 runs using different seed values (+ S.D.).

24

A

$$GluR + Glu \xrightleftharpoons[17{,}040/s]{9.18e^6 \, M/s} C1 \; GluR^*Glu + Glu \xrightleftharpoons[13{,}040/s]{5.68e^7 \, M/s} C2 \; GluR^*2Glu \xrightleftharpoons[1800/s]{8480/s} OpenGluR$$

$$5780/s \;\Big|\; 78/s \qquad 344/s \;\Big|\; 1.45/s \qquad 35.4/s \;\Big|\; 8/s$$

$$C3^*Glu + Glu \xrightleftharpoons[182.8/s]{2.54e^6 \, M/s} C4^*2Glu \xrightleftharpoons[380.8/s]{33.6/s} C5^*2Glu$$

Fig. 6. Simulated AMPA receptor activity using a model for GluR2. A. Reaction scheme for AMPA receptor activation from Bartol et al. (2015). B. Illustration of rod 1 spherule with bipolar cells (BP, purple and red), HCs (green and turquoise) and ribbon (semitransparent blue). AMPA receptors are shown as small white spheres. C. Simulated single vesicle AMPA receptor channel openings in four rod spherules compared with the average miniature excitatory post-synaptic current (mEPSC) recorded from mouse HCs (black trace $\pm$ S.D.). D. Individual simulations run with 4 different seed values in rod 3 (colored traces). Superimposed on these traces is the average AMPA receptor activity observed with simulations in the corresponding sphere model (n=25 seeds; black trace).

25

Fig. 7. Differences in release site location have an insignificant effect on EAAT5 anion channel activity. In all 4 rods, release was simulated at 3 different sites along each ribbon, one near the center (purple) and at two opposite edges (red and blue). Each trace shows the average $\pm$ S.D. of 25 simulations run with different seed values.
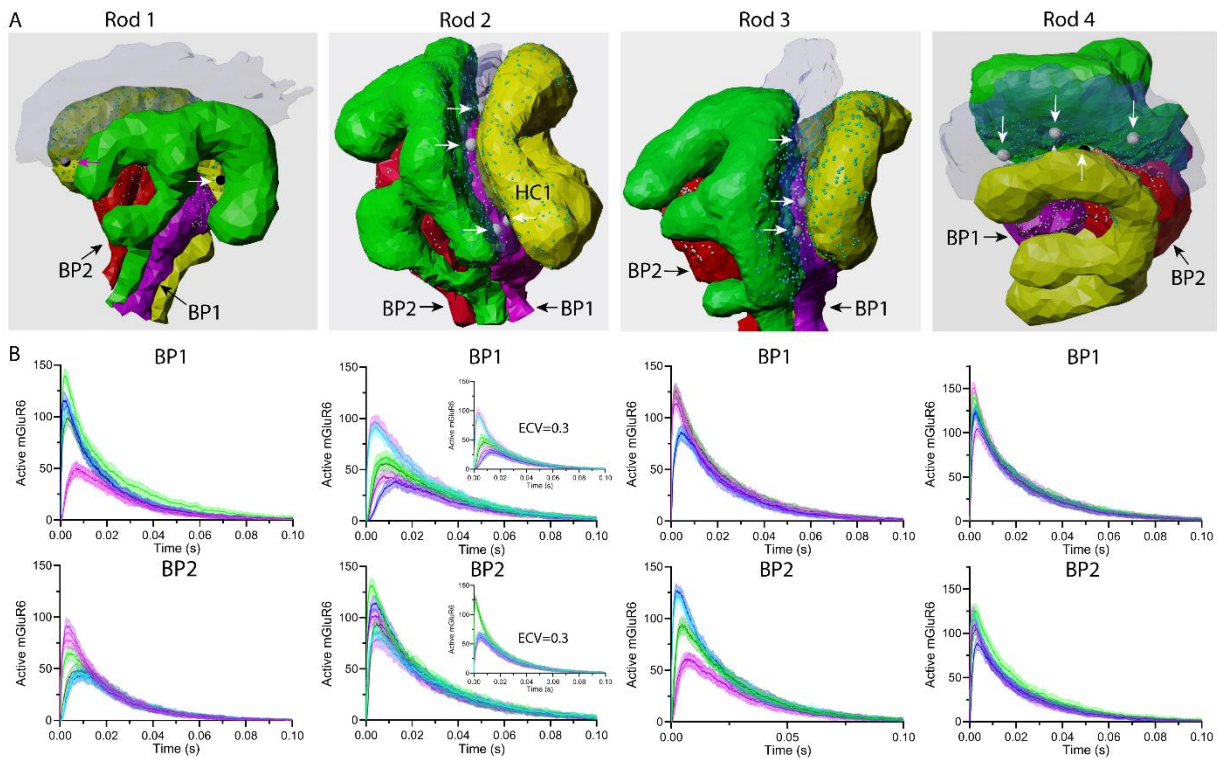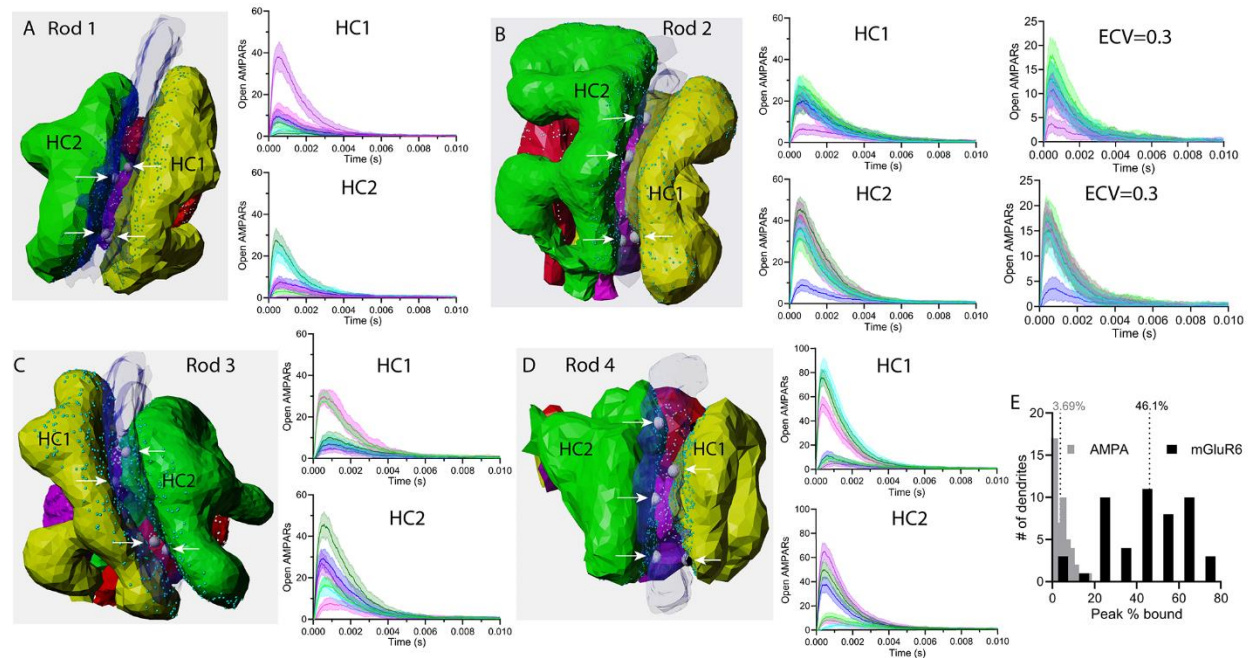

Fig. 8. Differences in release site location influence mGluR6 activity. A. Illustrations of rods 1-4 with their post-synaptic cells. Bipolar cells 1 and 2 are shown in magenta (BP1) and red (BP2), respectively. Ribbons are shown in transparent blue. Rod membranes have been removed for easier visualization. Visible release sites are indicated by arrows. The release site corresponding to the magenta trace in BP1

26

936   of rod 1 (panel B) is shown with a magenta arrow. B. Plot of the time course of mGluR6 activated by
937   release at six sites, 3 on each face of the ribbon. Responses of the two RPBs beneath each rod terminal
938   (BP1 and BP2) are plotted separately. Insets beneath Rod 2 shows the effect on mGluR6 activity of
939   increasing the extracellular volume fraction (ECV) of the synaptic cleft from 0.11 to 0.3. All graphs are
940   the mean $\pm$ S.D. of 25 simulations.

941

942   Fig. 9. Differences in release site location influence AMPA receptor activity. A. Rod 1 along with its post-
943   synaptic partners. HCs 1 and 2 are shown in yellow (HC1) and green (HC2), respectively. Ribbons are a
944   transparent blue. Rod membranes have been removed for easier visualization. Visible release sites are
945   denoted by arrows. Graphs plot time-dependent activation of AMPA receptors by release at six different
946   sites, 3 on each face of the ribbon. Responses of the two HCs beneath each rod terminal (HC1 and HC2)
947   are plotted separately. B. Illustration of rod 2 with graphs of AMPA receptor activity in HC1 and HC2.
948   Site-to-site variability remained after increasing the extracellular volume fraction (ECV) from 0.11 to 0.3.
949   C. Illustration of rod 3 with graphs of AMPA receptor activity in HC1 and HC2. D. Illustration of rod 4
950   with graphs of AMPA receptor activity in HC1 and HC2. E. Frequency histogram of the peak percentage
951   of activated HC AMPA (gray) and RBP mGluR6 receptors (black) produced by release at different ribbon
952   sites. For these simulations, we increased the number of AMPA receptors on each HC from 200 to 500.
953   Graphs plot the mean $\pm$ S.D. of 25 simulations.

27

|	Rod 1	Rod 2	Rod 3	Rod 4
Surface Area (μm^2)	29.15	27.67	32.29	26.13
Volume (μm^3)	5.94	5.024	6.576	4.771
Faces	6,580	14,498	57,802	30,384
Cleft Volume (μm^3)	0.564	0.572	0.6056	0.448
Extracellular cleft volume (μm^3)	0.1125	0.06	0.074	0.057
Extracellular volume fraction	0.2	0.11	0.12	0.13
Horizontal cell dendrite 1				
Surface Area (μm^2)	2.758	3.272	2.726	2.382
Volume (μm^3)	0.1674	0.1945	0.1763	0.114
Faces	2040	4754	2388	1914
Horizontal cell dendrite 2				
Surface Area (μm^2)	2.827	3.123	3.213	2.272
Volume (μm^3)	0.1894	0.1758	0.2228	0.1337
Faces	1088	7020	5530	2418
Bipolar cell dendrite 1				
Surface Area (μm^2)	0.7964	1.2167	1.0288	1.1962
Volume (μm^3)	0.03475	0.07234	0.06593	0.07867
Faces	662	3084	5038	602
Bipolar cell dendrite 2				
Surface Area (μm^2)	0.6539	1.041	1.0622	1.17
Volume (μm^3)	0.03208	0.069	0.06686	0.06456
Faces	1422	714	4832	568
Bipolar cell dendrite 2b				
Surface Area (μm^2)	0.6792			
Volume (μm^3)	0.0276			
Faces	1732			

954

955   Table 1. Details of mesh structures of rods, HC dendrites, and RBP dendrites used for simulations.

28

Activated mGluR6

	With 3,000 EAAT5				No EAAT5	
	Peak % bound	τ_{fast} (ms)	% fast	τ_{slow} (ms)	Peak % bound	τ (ms)
Rod 1	42.1	4.8	33	24	53.9	20.4
Rod 2	40.6	4	29	40.1	58.3	42.9
Rod 3	39.3	7.2	18	30	50.8	26.7
Rod 4	53.5	5.4	48	28.2	56.4	26.2
Sphere	98.6			10.1	99	6.6
(volume of rods 2-4)						

Table 2. Best fit parameters from Fig. 6 plotting mGluR6 activity evoked by single vesicle release events in rods 1 to 4, as well as a sphere model.
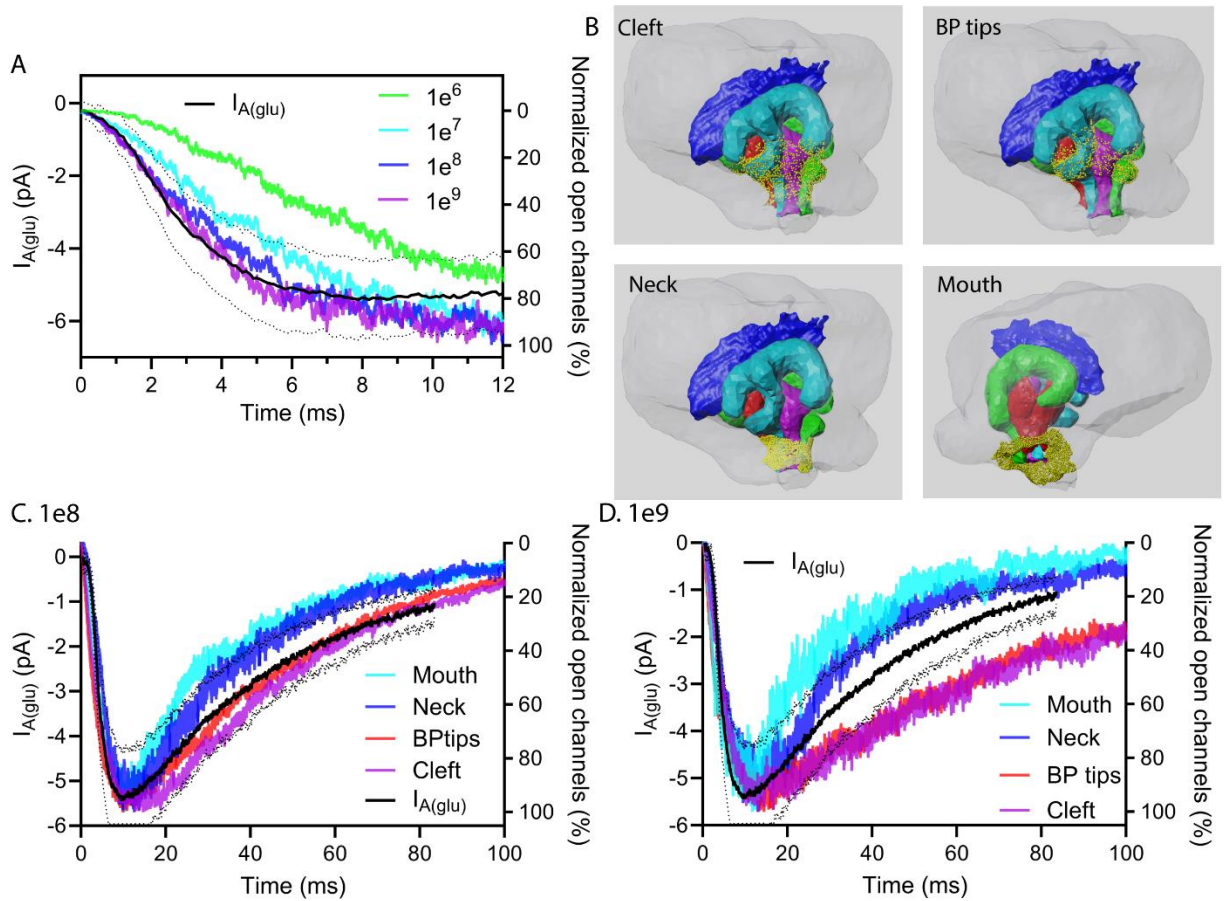
Supplemental Fig. 1. EAAT5 parameters and placement. Comparison of ON rates for glutamate binding to EAAT5 (1 x10^6 M/s to 1 x 10^9 M/s). Black trace shows the average $\pm$ S.D. single vesicle $I_{A(glu)}$ in rods. B. Illustration of EAAT5 (yellow puncta) placement in four different regions of the synaptic invagination: throughout the cleft (Cleft), adjacent to bipolar cell dendritic tips (BP tips), the neck of the invagination (Neck), and just outside the mouth of the invaginating synapse (Mouth). Ribbon is colored dark blue. HCs are green and turquoise. RBPs are red and purple. C. Simulated EAAT5 anion channel activity after placing EAAT5 in the different regions shown in B with a glutamate ON-binding rate 1 x 10^8 M/s. D. Simulated EAAT5 anion channel activity with placement in various locations using an ON rate of 1 x 10^9 M/S. Traces show the average of 12 simulations run with different seed values.

29
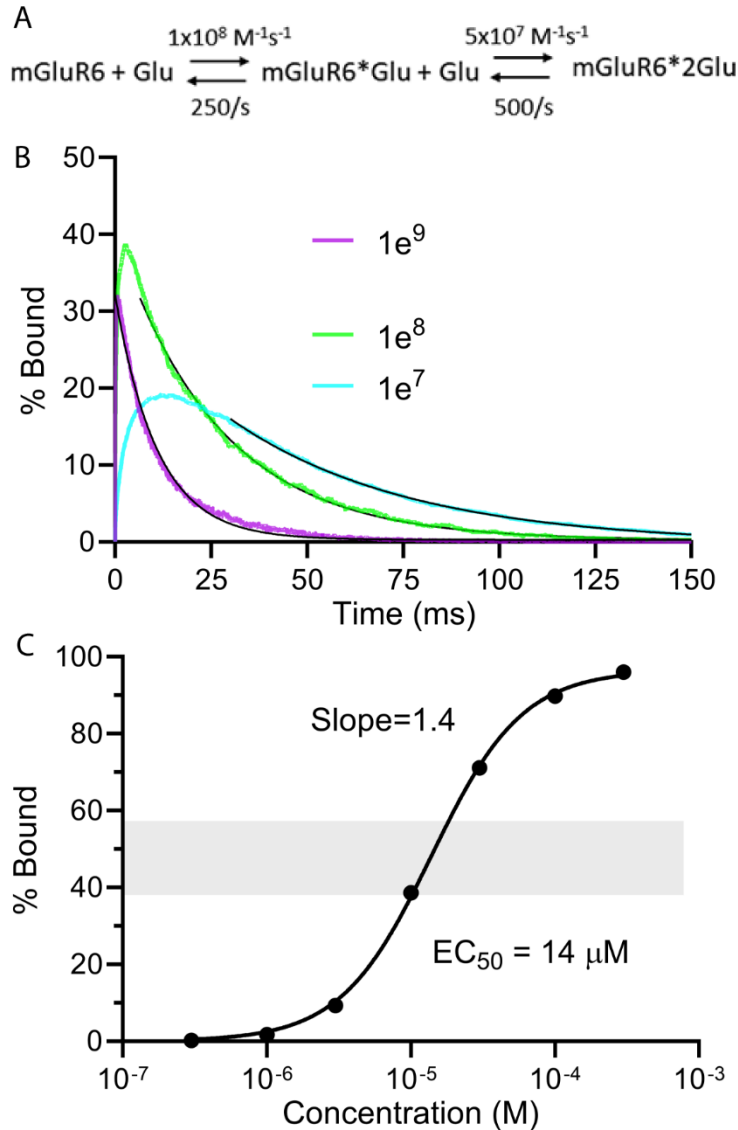
Supplemental Fig. 2. Kinetics of glutamate binding to mGluR6. A. Kinetic scheme for glutamate binding to mGluR6. The activated receptor was considered the doubly bound state (mGluR6*2Glu). B. Kinetics of mGluR6 activation (i.e., doubly bound mGluR6) are shown for different glutamate binding rates. For 1 x 10^9, 1x10^8, and 1x10^7 M/s, the corresponding OFF rates for unbinding of the last glutamate molecule were 2500/s, 250/s, and 25/s, respectively. The later portion of the decay was fit with a single exponential: 1 x 10^9 M/s, 11.0 ms; 1x10^8 M/s, 26.7 ms; 1x10^7 M/s, 46.7 ms. Simulations show the average of 12 seed values run in rod 3 in the presence of 3,000 EAAT5. C. Plot of steady state mGluR6 activation as a function of glutamate concentration using the model parameters in A. Data were fit with a sigmoidal Hill function: EC_{50} = 14 μM. Hill slope = 1.4.